Tectonics®

RESEARCH ARTICLE
10.1029/2021TC006955

Key Points:

- Heterogeneities in the detachment layer favor strain localization and partitioning in fold-and-thrust belts
- Diapirs and frontal pinch-outs favor deformation stagnation and the deposition of gravitational bodies
- Our models contribute to better understand natural cases of progressive arcs that include heterogeneities in their detachment layer

Supporting Information:

Supporting Information may be found in the online version of this article.

Correspondence to:

A. Jiménez-Bonilla,
ajimbon@upo.es

Citation:

Jiménez-Bonilla, A., Ramos, I. E., Díaz-Azpíroz, M., Balanyá, J. C., & Crespo-Blanc, A. (2022). Strain partitioning and localization due to detachment heterogeneities in fold-and-thrust belts of progressive arcs: Results from analog modeling. *Tectonics*, *41*, e2021TC006955. https://doi.org/10.1029/2021TC006955

Received 25 JUN 2021
Accepted 7 NOV 2022

Strain Partitioning and Localization Due To Detachment Heterogeneities in Fold-and-Thrust Belts of Progressive Arcs: Results From Analog Modeling

Alejandro Jiménez-Bonilla[1], Inmaculada Expósito Ramos[1], Manuel Díaz-Azpíroz[1], Juan Carlos Balanyá[1], and Ana Crespo-Blanc[2]

[1]Departamento de Sistemas Físicos, Químicos y Naturales, Universidad Pablo de Olavide, Seville, Spain, [2]Departamento de Geodinámica-Instituto Andaluz Ciencias de la Tierra, Universidad de Granada-CSIC, Granada, Spain

Abstract Although most arcuate orogens are deformed as progressive arcs—curvature is acquired during shortening-, they have been scarcely simulated by analog modeling. To investigate factors that control the growth of progressive curves in fold-and-thrust belts, we developed seven analog models where the backstop shape changed over time, and distinctive geometric heterogeneities were set in the detachment layer. These heterogeneities, often described in natural cases, include diapirs, thickness lateral variations (including pinch-outs) of the viscous detachment layer as well as frontal pinch-outs. Our results show that strain was partitioned between shortening structures showing radial transport directions, and both normal and oblique strike-slip faults that accommodated arc-lengthening. The location of any heterogeneity conditioned the nucleation of structures and thus, the wedge evolution and its resulting geometry. The presence of both diapirs and frontal silicone pinch-outs favored the stagnation of the deformation front, and the subsequent wedge thickening up to reach the supercritical angle. Both diapirs and thickness lateral variations of the viscous layer localized arc-parallel stretching. In addition, their configuration determined the amount and distribution of salients and recesses along the arcuate belt, diapirs and more frictional detachments favoring thicker wedges and less frontal propagation. The differential displacement between salients and recesses was accommodated by strongly partitioned transfer zones, localized by the boundaries between distinctive detachment domains. These results may be useful to investigate geometric and kinematic changes along natural progressive arcs such as the Gibraltar, Sulaiman and Zagros cases.

Plain Language Summary Even though most of arcuate orogens acquire their curvature at the same time as they build up—progressive arcs-, they are poorly studied. Recent analog models helped to study these arcs by using a plastic strip that protrudes in plan view and pushes from behind the analog material (Jiménez-Bonilla et al., 2020, https://doi.org/10.3389/feart.2020.00072). They used uniform thickness layers of sand and silicone as analog materials to reproduce the brittle-ductile behavior in the upper crust, being the silicone the weak layer where the detachment localizes. In this work, we added to the silicone layer heterogeneities (diapirs, silicone thickness variations and silicone pinch-outs) in order to understand how they influence the nucleation and kinematics of structures. Both diapirs and silicone pinch-outs perpendicular to the apex movement favored that deformation slows down and the wedge thickens until frontal collapse. The presence of any heterogeneity favors the nucleation of structures. When silicone bands are parallel to the apex movement, different structural styles along the fold-and-thrust belt generated. Low silicone thicknesses favor thicker wedges and less frontal propagation. These models are useful to understand the development of orogens whose fold-and-thrust belt detachment includes heterogeneities such as the Zagros, the Betics or the Sulaiman arc.

1. Introduction

Orogenic arcs may be classified based on their kinematic evolution into: (a) primary arcs, whose curvature is inherited from the early stages; (b) oroclines, formed by bending of an initial straight belt and (c) progressive arcs, which acquire their curvature gradually as the arc develops (Weil & Sussman, 2004). In addition to arc kinematics, the degree of curvature of their fold-and-thrust belts (external zones) may be conditioned also by the rheological properties and geometry of its detachment layer located at the upper crust. For instance, the detachment layer behavior—brittle or ductile—has been proven to control fold-and-thrust belt vergence (e.g., Agarwal & Agrawal, 2002), whereas depocenters of the detachment-related rock formation localize the salients generation

in plan view (Macedo & Marshak, 1999; Yonkee & Weil, 2015). However, the influence that detachment layer heterogeneities exert on the tectonic features that progressive arcs acquire as deformation proceeds is still a matter of study. In this respect, lateral variations of the detachment layer may control the kinematics of structures, the strain localization and the strain partitioning modes operating in progressive arcs (e.g., Allerton, 1998; Macedo & Marshak, 1999; Marshak, 2004; Weil & Sussman, 2004).

In this regard, analog modeling is a suitable approach to delve into the nucleation and development of arcuate fold-and-thrust belts. Both primary arcs and oroclines have been intensively modeled by analog experiments (e.g., Crespo Blanc & González Sánchez, 2005; Lickorish et al., 2002 for primary arcs; Ghiglione & Cristallini, 2007; Pastor-Galán et al., 2012 for oroclines). Nevertheless, most natural cases of fold-and-thrust belts seem to evolve as the "progressive arc" type of Weil and Sussman (2004). Few analog models of progressive arcs have been performed apart from some piedmont-type models, which reproduced divergent transport directions. Although these models also provoke a foreland-ward increasing arc-parallel extension, they do not reproduce a true fold-and-thrust belt (Gautier et al., 1999; Jiménez-Bonilla, Crespo-Blanc, et al., 2017; Merle, 1986, 1989).

To characterize the evolution of fold-and-thrust belts in progressive arcs, Crespo-Blanc et al. (2017) and Jiménez-Bonilla et al. (2020) presented an apparatus that produces arcs using a rigid backstop whose shape changes as the arc develops. This design differs from those used in previous analog studies, where the shape of the rigid backstop stayed the same throughout the growth of the arc. By using this setting, we obtained fold-and-thrust belts characterized by radial thrusting together with arc-parallel stretching accommodated by normal faults and conjugate strike-slip faults. These faults allowed the individualization of blocks that underwent vertical-axis rotations at both arc limbs (Crespo-Blanc et al., 2017; Jiménez-Bonilla et al., 2018, 2020). These kinematic features resemble those observed in fold-and-thrust belts of Mediterranean arcs, especially the Gibraltar arc (Cifelli et al., 2008; Crespo-Blanc et al., 2016, 2018; Marshak et al., 1982).

The experiments of Jiménez-Bonilla et al. (2020) used a uniform-thickness silicone layer—i.e., the weak layer-at the bottom of the analog pack, which simulated a homogeneous, viscous detachment as often observed flooring fold-and-thrust belts. However, the distribution of this viscous layer is neither uniform nor homogeneous in natural cases, which may be key to interpreting structural style, including cross-section and plan view geometries, strain localization and evolution along time of fold-and-thrust belts. This heterogeneous distribution is observed in many natural cases of progressive arcs by the presence of changes in the frictional properties of the detachment layer (e.g., Gibraltar arc: Vera, 2004; Chalouan et al., 2008), variations in the thickness of the detachment layer (e.g., Gibraltar arc: Vera, 2004; Crespo-Blanc, 2008; Crespo-Blanc et al., 2012; Barcos et al., 2015; Jiménez-Bonilla et al., 2015, 2016; 2017b), the presence of pre-deformational diapirs (e.g., Gibraltar arc: Nieto et al., 1992; Pedrera et al., 2014; Jiménez-Bonilla et al., 2015, or Sulaiman arc: Rubinat et al., 2013; Kokinou et al., 2017; Najafi et al., 2018; Hassanpour et al., 2018) and/or the existence of detachment layer pinch-outs (e.g., Zagros: Bahroudi & Koyi, 2003; Burkhard & Sommaruga, 1998; Hindle & Burkhard, 1999; Livani et al., 2018; McQuarrie, 2004; Ruh et al., 2017).

Accordingly, in this work, we show the results of analog models of progressive arcs simulated with a protruding indenter, that is, a similar set-up as Jiménez-Bonilla et al. (2020), although we introduced differences in the geometry of the detachment layer: (a) lateral variations in the silicone thickness, (b) silicone pinch-outs both perpendicular and parallel to the apex movement direction and (c) pre-deformational diapirs of silicone with different sizes and distribution. The obtained results allow us to inquire about the role of these different settings in the resulting structural trend-line pattern, wedge geometry, strain localization and tectonic style of different fold-and-thrust belts in natural cases of progressive arcs.

2. Methodology

2.1. Material Properties and Scaling

Experiments were carried out in the Analog Modeling Laboratory of the Geodynamics Department-IACT of the University of Granada-CSIC (Spain). In these experiments, we reproduce the brittle-ductile conditions of the upper crustal sedimentary cover with sand and silicone as analog materials (Jiménez-Bonilla et al., 2020).

Table 1
Geometrical Parameters of the Resulting Fold-And-Thrust Belts in Plan View of Models 1 to 7 and Models 4.1 and 4.2 (Jiménez-Bonilla et al., 2020)

	PG	AF	AI	Sin	Frontal FTB width (cm)	Maximum lateral FTB width (cm)
Model 1	1.02	1.00	0.13	1.10	19.5	24.2
Model 2	1.18	1.00	0.42	1.13	24.3	14.5
Model 3	0.75	1.02	0.80	1.07	8.5	20.5
Model 4	0.94	1.03	0.91	1.19	13.2/36.2 (S)	12.5/18.3 (S)
Model 5	1.23	1.00	0.23	1.07	27.5	8
Model 6	0.99	1.01	0.42	1.08	18/12.2 (S)	6.7/8.5 (S)
Model 7	0.65	1.04	0.14	1.36	10.5	13.1
Model 4.1	0.94	1.00	0.22	1.11	15.5	13.2
Model 4.2	0.98	1.02	0.37	1.16	30.5	16.5

Note. (S): Higher Thickness of the Silicone Layer, PG: protrusion grade, AF: asymmetry factor, AI: asymmetry index, Sin: sinuosity, FTB: fold-and-thrust belt (S): silicone band.

Dry and rounded quartz grains, with sizes from 0.2 to 0.3 mm, angle of internal friction 37° and density 1.77 g/cm^3, simulate the strain rate-independent behavior of most of brittle sedimentary rocks (e.g., Cobbold et al., 2001; Wu & McClay, 2011).

The strain rate-dependent flow of evaporitic rocks and overpressured shales are reproduced by silicone (Schellart & Strak, 2016; Schellart et al., 2004). The silicone putty used in all experiments was the Rhodosil Gum FB of Rhone-Pulenc. It behaves as a Newtonian material at the experimental strain rates (10^{-6} s^{-1}). The density is δ_{dM} = 0.98 g/cm^3 and the viscosity $\eta_M = 5 \times 10^4$ Pa s at room temperature (Funiciello et al., 2003).

The scaling is described in Jiménez-Bonilla et al. (2020) for the Gibraltar arc as a natural case of progressive arc. See Table 1 of this work for scaling factors.

2.2. Model Setup

For the purpose of comparison, we have used the same model set up of progressive arcs of Jiménez-Bonilla et al. (2020): a 100 × 70 cm sand-silicone box that includes a 62 cm wide gate (Figures 1a and 2). The lateral and frontal boundaries of the experiments were confined by sand, and all models were totally covered by a sandpack multilayer to reach 2-cm of total thickness (Figures 1a and 1b). The plastic strip used as indenter is pushed from behind at its apex by a screw attached to a motor drive. This strip has the capability to deform by bending in plan view while it is pushed through the gate. Figures 1c and 1d show the indenter deformation during our experiments. It deforms in the same way independently whether the analog material is

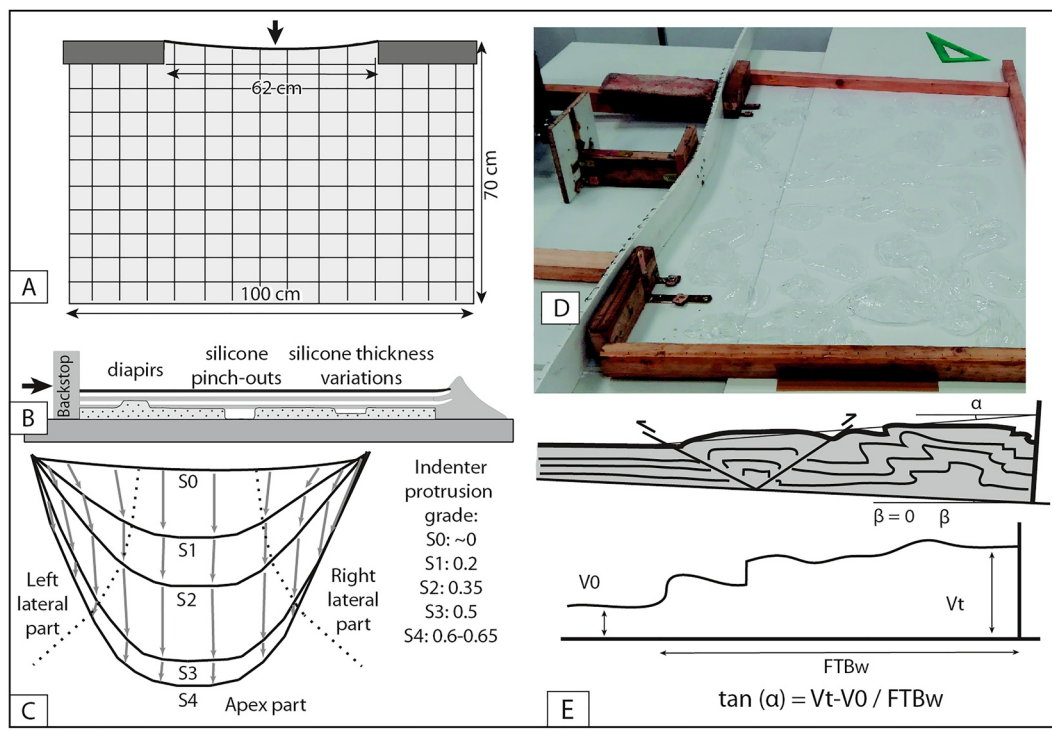

Figure 1. (a and b) Simplified sketch of the experimental apparatus and model setup in plan view and cross-section. (c) Shape and particle displacement path of the deformable indenter for different deformation stages (S1 to S3) as in Jiménez-Bonilla et al. (2020). (d) Oblique picture of the model set up showing the indenter geometry at S0 (e) Sketch of the wedge and the measurement of α and β in our models. FTBw: fold-and-thrust belt width; Vt: Vertical thickness; V0: Vertical thickness outside the FTB.

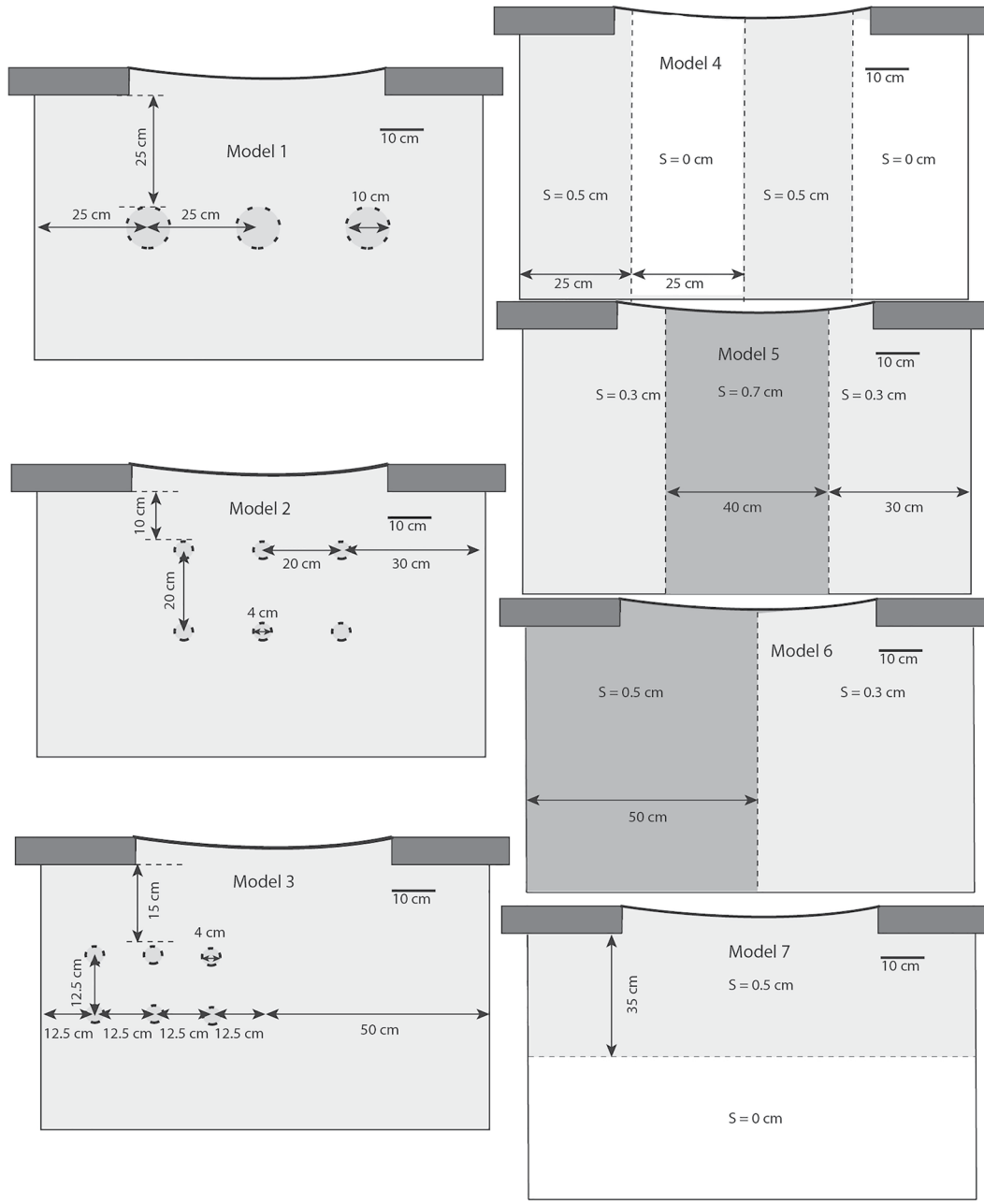

Figure 2. Model set ups of Models 1 to 7 showing the geometry of the detachment layer.

present or not. The analog pack is deformed in curved fold-and-thrust belts whose shortening is maximum in the apex zone, decreasing toward the lateral parts of the models (Figures 1c and 1d; see Jiménez-Bonilla et al., 2020 for further information).

The indenter used in the experiments moved at a constant speed, which is between 0.65 and 0.8 cm/hr depending on the experiment. These velocities are scaled on convergence velocities of natural cases (e.g., Gibraltar arc) and, within this range of velocities, the silicone behaves as a Newtonian material (see Jiménez-Bonilla et al., 2020 for scaling). The maximum amplitude reached by the indenter was between 35 and 40 cm at the apex part, as in previous experiments (Jiménez-Bonilla et al., 2020). We stopped the models when the apex moved 5 cm without the nucleation of any new structure.

Table 2
Geometrical Parameters of the Resulting Wedges and Maximum Angle Between Kinematic Vectors of Models 1 to 7 and Models 4.1 and 4.2 (Jiménez-Bonilla et al., 2020)

	Maximum FTB thickness in the apex (cm)	Alpha angle in the apex (º)	Lateral FTB maximum thickness (cm)	Alpha angle in the lateral FTB	Maximum angle between kinematic vectors (º)
Model 1	6.5 (325%)	1	4 (200%)	4.6	150
Model 2	6 (300%)	9.6	4.5 (225%)	9.6	85
Model 3	8 (400%)	35	4 (200%)	5.7	75
Model 4	8 (400%)/6 (300%) (S)	24.2/6.2 (S)	5 (250%)/7 (350%) (S)	13.5/15.1 (S)	90
Model 5	6 (300%)	8	5.5 (275%)/4 (200%) (S)	23.2	90
Model 6	5.5 (275%)/4 (200%) (S)	10.9/9.1 (S)	6 (300%)/4 (200%)	25.1 (S)/16.2	120
Model 7	10 (500%)	37.2	5 (250%)	22.9	75
Model 4.1	6.5 (325%)	16.2	6.5 (325%)	18.7	95
Model 4.2	7 (350%)	9.1	5 (250%)	10.2	100

Note. (S): Higher Thickness of the Silicone Layer, FTB: fold-and-thrust belt.

2.3. Types of Experiments

Our experiments were intended to obtain a preliminary view on how specific initial configurations of the underlying ductile layer may influence both the structural style and the tectonic evolution of fold-and-thrust belts of progressive arcs. We have made seven different experiments arranged into three groups (Figures 1b and 2):

In Models 1 to 3, we explore the effect of pre-deformational diapirs on the strain localization and modes of strain partitioning during fold-and-thrust belt building. This first group is characterized by the occurrence of 0.5 cm thick diapirs added to the initial 0.5 cm thick silicone layer. Three different models were made with variations in size, number and arrangement of silicone diapirs: three diapirs of 10 cm diameter in Model 1, and six diapirs of 4 cm diameter in Models 2 and 3 (Figure 2). In Model 3 all diapirs were located at the left side of the analog pack. See S0 of each model in Figure 2 to see the distribution of silicone diapirs.

Models 4 to 6 simulate thickness variations on the basal ductile layer defining homogeneous pre-deformational bands parallel to the movement of the hinterland in the arc apex. We study the different strain partitioning modes between bands and the effect of strain localization at their boundaries. S0 in Figure 2 shows silicone thicknesses and dashed lines mark the boundaries between the resulting bands. In Model 4, the analog pack presents four bands, 25 cm wide, which were underlain from left to right by 0.5, 0, 0.5, and 0 cm thick silicone layers, thus generating silicone pinch outs (Figure 2). In Model 5, there are three bands, being the central one thicker and wider (0.7 cm thick and 40 cm wide) than those located at the arc limbs (0.3 cm thick and 30 cm wide; Figure 2). In Finally, the detachment level of Model 6 consists of two bands of silicone, being 0.5 and 0.3 cm thick in the left and the right arc limbs, respectively (Figures 1b and 2).

Model 7 reproduces a ductile layer pinch-out, located at the base of the FTB column, which trends perpendicular to the movement of the hinterland in the arc apex, hereafter called as frontal pinch-out. Here, we study the effect of such pinch-out in the resulting structural trend-line pattern and in the wedge geometry, compared with those of the previous models. The silicone layer is 0.5 cm thick where it is present. The location of the silicone pinch out is shown with a dashed line in Figures 1b and 2.

2.4. Modeling Procedures

A reference 3 × 3 cm grid was sieved on top of the analog pack to allow kinematics analyses. The progressive deformation was monitored by time-lapse photography of the model surface every 10 min, and its final geometry was also recorded by oblique photographs. Representative cross-sections of the deformed models were made in some experiments. In others, the sand was carefully removed to observe the final 3D-geometry of the silicone.

Tables 1 and 2 show the parameters used to characterize the resulting fold-and-thrust belt geometry in order to remark the principal qualitative differences between cases. For descriptions, we have distinguished between the

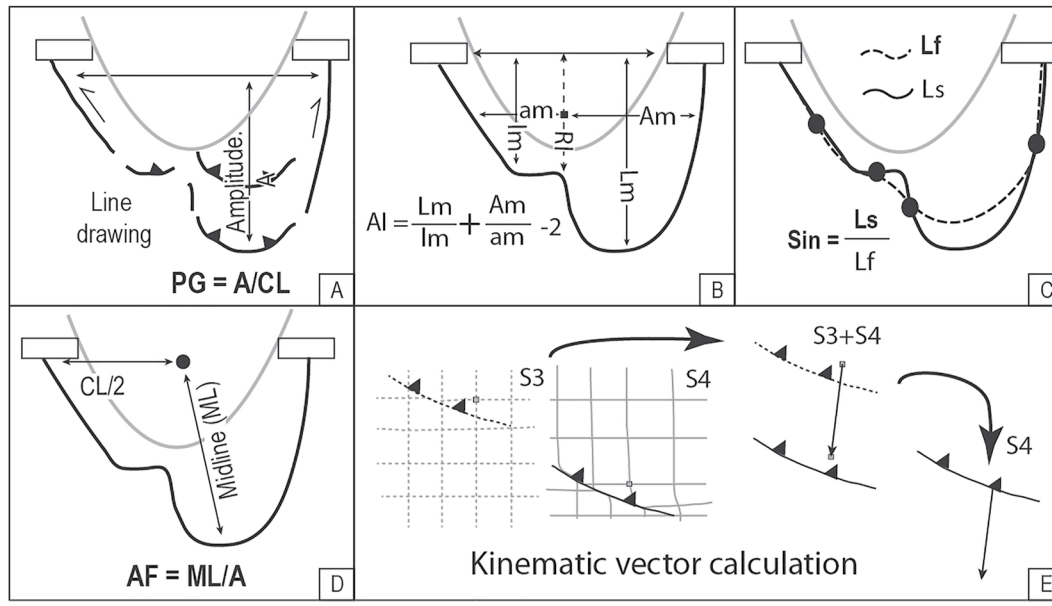

Figure 3. (a–d) Sketches of terminology and calculation of the geometrical parameters used in the paper: Protrusion grade (PG), Assymmetry index (AI), Sinuosity index (Sin) and Asymmetry factor (AF). (e) Sketch of the measurement of the displacement vector (arrow) between S3 and S4.

apex and lateral (right and left) parts as indicated in Figure 1c. We define the *fold-and-thrust belts width* (FTBw in Figure 1e) as the horizontal distance between the indenter and the frontal thrust, measured perpendicular to the indenter and omitting border effects. We also measured its *maximum vertical thickness* (Vt in Figure 1e) at the end of all experiments with a millimeter graduated pin. The location of these measurements is indicated with stars in Figures 4, 6, and 8 The wedge geometry is described by the wedge taper angle (Figure 1e; Dahlen et al., 1984, 1990), which is the sum of angles β (detachment angle) and α (surface slope). Given that all our models exhibit a horizontal base, β is always 0°, thus the wedge taper angle equals α in these experiments. We estimated the angle α as the difference between Vt and *V0* (the thickness outside the FTB) divided by FTBw (Figure 1e), excluding border effects. We corroborated these values by measuring α directly from cross-sections when possible.

In plan view, we calculated the *protrusion grade* (PG; Marshak, 1988; Macedo & Marshak, 1999, Figure 3a) as the ratio between amplitude and chord length. To measure the asymmetry, we used two indexes, which are sensitive to different kinds of asymmetry: (a) the *asymmetry factor* (AF, Macedo & Marshak, 1999) is the ratio between the midline and the amplitude and it is highly sensitive to the presence of protruded lateral salients (Figure 3d); (b) in order to include different types of asymmetries, we define the *asymmetry index* (AI) as:

$$AI = [\,(Lm/lm) + (Am/am)\,] - 2$$

We define the reference line as the segment parallel to the apex movement between the middle point of the gate and the deformation front (dashed line Rl; Figures 1d and 3b). *Lm* and *lm* are defined as the segments parallel to the reference line—i.e. parallel to the transport direction-whose starting points are in the middle between the reference line and the gate tips (Figure 3b). Lm and lm are, respectively, the longest and shortest segments. *Am* and *am* are the segments perpendicular to the reference line between the central point of the reference line and the lateral deformation fronts, being Am and am the longest and the shortest ones, respectively (Figure 3b). Given that the ideal symmetric arc would yield a value of 0, AI increases progressively with higher asymmetries.

We measured the *sinuosity* of the frontal fold-and-thrust belt (Sin, Figure 3c) by comparing the lengths of the outer fold-and-thrust front (*Ls*) with that of the median line Lf. The *median line* is defined as the curve that follows the arc outer front but it is smoothed out by connecting the inflection points along its salient and recesses (Figure 3c). Hence, Sin values close to 1 correspond to non-sinuous arcuate fold-and-thrust belts, progressively

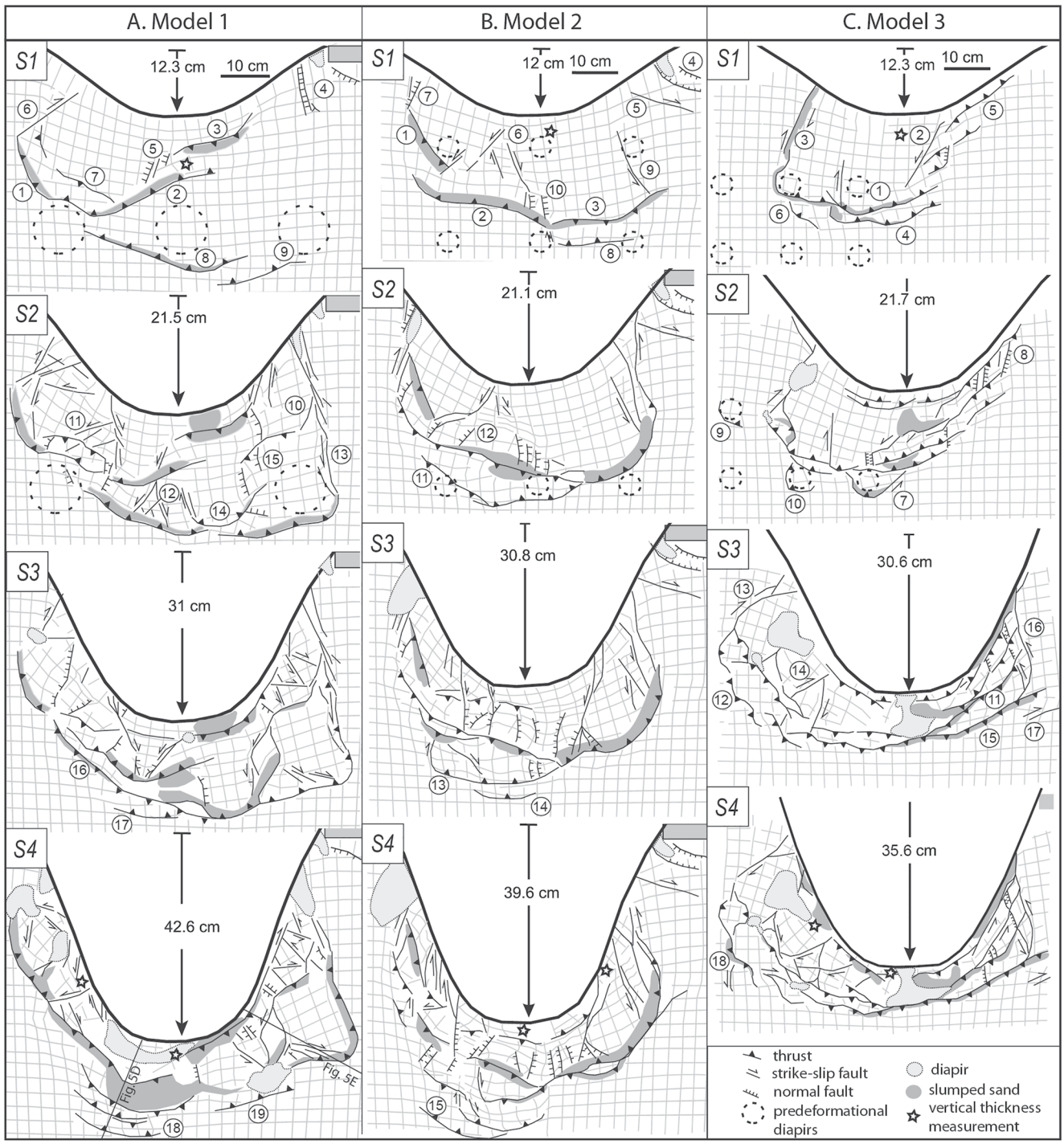

Figure 4. (a–c) Line drawings of the stages S1 to S4 of models with diapirs (Models 1 to 3). Diapirs geometry and location are indicated by dashed lines at S1. The numbering indicates the relative chronology of structures. The apex displacement is indicated for each stage.

increasing with more complex geometries. We used the terms *salient* and *recess* in the sense of Macedo and Marshak (1999).

Figures 9a and 9b show the values of PG, AF, AI and Sin at the end of the experiments for Models 4.1 and 4.2 of Jiménez-Bonilla et al., 2020 as well as for our Models 1 to 7, respectively. The evolution of PG, AF and AI from S1 is shown in Figure S1.

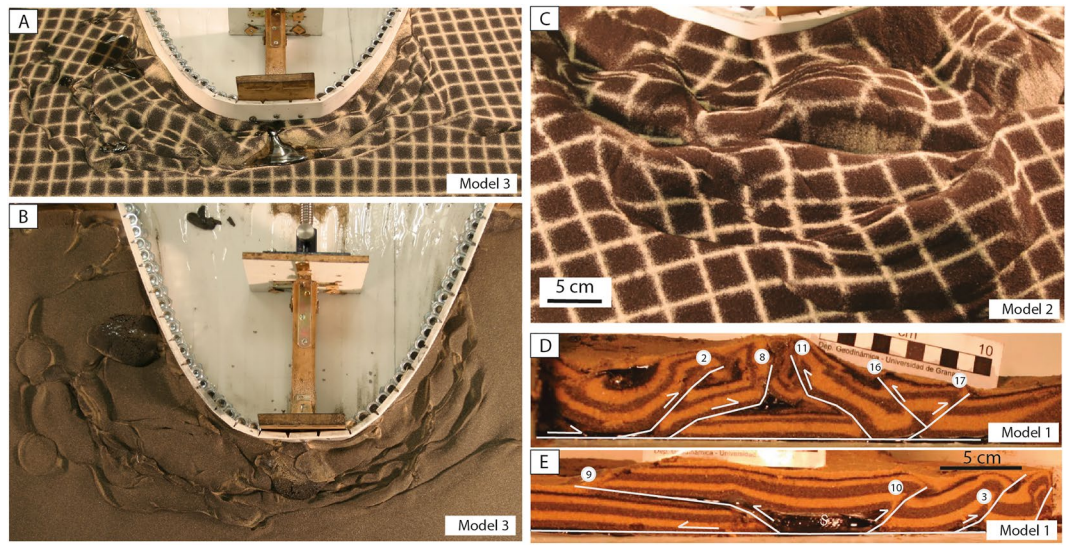

Figure 5. Photographs of Models 1 to 3. (a and b) Pictures in plan view of Model 3 at the end of the experiment and the silicone topography, respectively. (c) Detailed picture of arc-perpendicular normal faults and their control on the relief in Model 2 (d) Cross-sections subparallel to the transport direction of Model 1. See Figure 4a for cross-section locations. All pictures were taken at the end of the experiments.

For kinematics analyses, we represented vectors on selected structures at the S4 as the mean direction and total displacement of hanging-wall movement from S3 to S4 stages, measured from the grid displacement (Figure 3e). We show the related kinematic vectors for previous models 4.1 and 4.2 of Jiménez-Bonilla et al., 2020 and for our models 1 to 7 (see their Figures 10a and 10b, respectively). The maximum angle between kinematic vectors refers to the total range of thrust directions of both arc branches. At the last stage of the experiments, vertical axis rotations were measured using grid markers.

2.5. Model Limitations

Due to the large dimensions of the analog pack used for these models (100 × 70 cm), taken to avoid border effects, there are some unavoidable heterogeneities in the preparation and in the development of the experiments: (a) there are small variations of the sand or silicone thickness and (b) in some experiments there is a slight deviation of the indenter movement from the ideal displacement, especially in Models 1 to 3 (See videos 1 to 3). In all cases, although these heterogeneities affect neither the strain partitioning modes nor the strain localization, they may affect locally the distribution of thrusts, backthrusts, strike-slip, and normal faults, as it occurs in previous analog models of progressive arcs (Jiménez-Bonilla et al., 2020). In Section 3, we will focus on the key aspect of each type of model.

Regarding α values, previous works have highlighted the exaggerated topography and α values produced in analog models, which are attributed to: (a) the absence of isostatic compensation, (b) the need for a correction factor in the scaling of density contrast, (c) the boundary conditions, and (d) the absence of erosion (Schellart & Strak, 2016). α values are between 2° and 11° both in numerical models and in those analog models made up of sand on Mylar sheets with coefficient of basal friction = 0.3 and β = 0° (Dahlen et al., 1984; Davis et al., 1983; Ruh et al., 2012). When using a viscous detachment, the taper angle diminishes to less than 1° (Costa & Vendeville, 2002; Ruh et al., 2012), even though it is higher than in natural cases.

3. Results

Regardless of their original configuration, our models show certain similarities in terms of strain partitioning and structural evolution. Although their geometric complexity varies from each other, all analog packs are deformed in curved fold-and-thrust belts with salients and recesses in plan view (Figures 4–9 and Table 1). Thrusts and backthrusts, the latter favored by the viscous substrate, accommodate shortening that define a radial pattern.

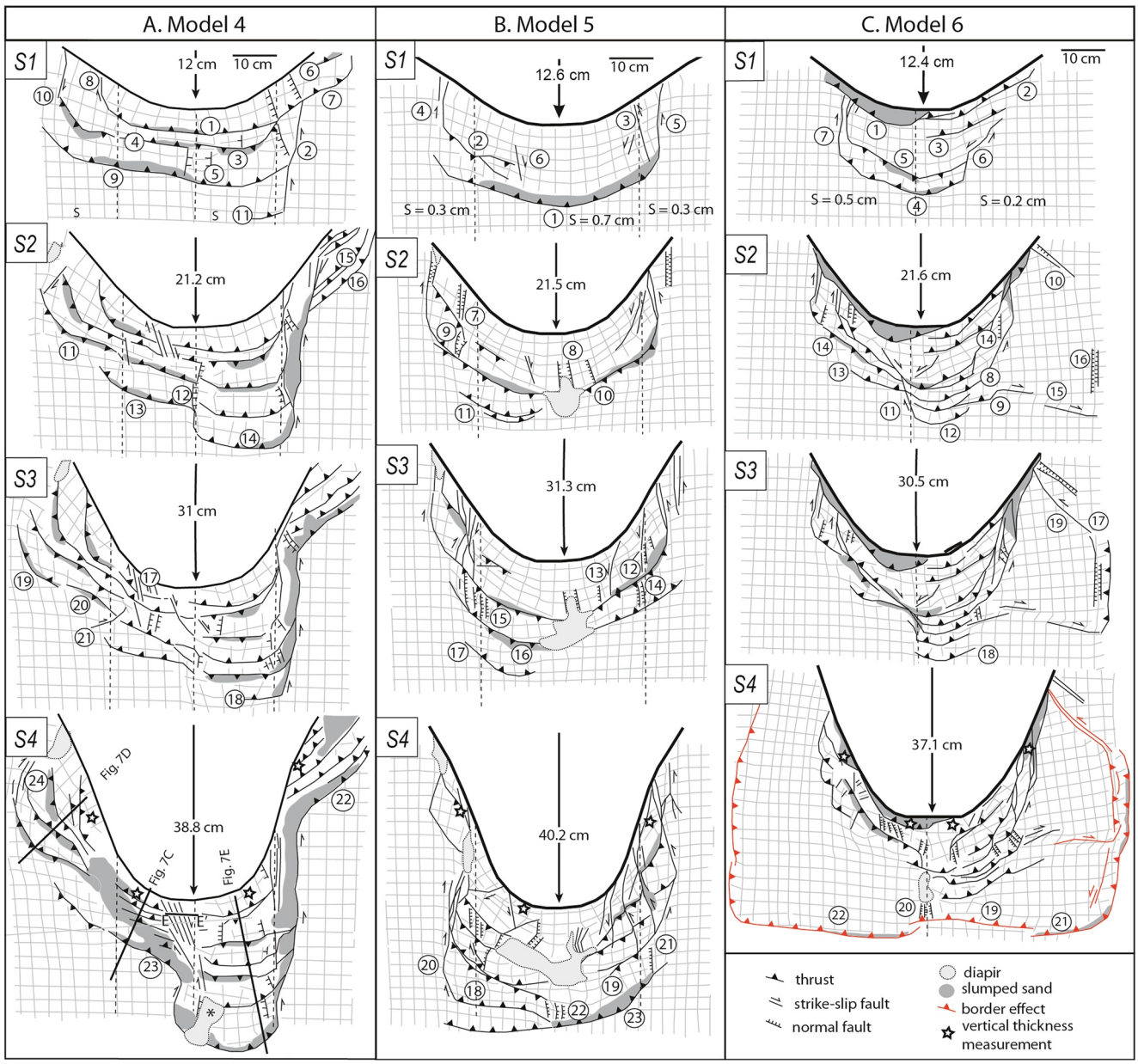

Figure 6. (a–c) Line drawings of the stages S1–S4 of models with silicone bands oriented parallel to the apex movement (Models 4–6). Dashed lines indicate silicone boundaries between bands and silicone thickness are indicated. The numbering indicates the relative chronology of structures. The apex displacement is indicated for each stage.

Most of these thrusts are oblique faults as deduced from the angle between their strikes and related kinematic vectors (Figure 10b). Transpressive bands usually develop at the lateral parts of the models. Arc-parallel stretching is accommodated by normal faults and conjugate strike-slip faults (Figure 10b). These faults provoke the along-strike fold-and-thrust belt segmentation and the individualization of blocks that rotate independently, being clockwise and counterclockwise in left and right arc limbs, respectively (Figures 4, 6, and 8). At the last stage of deformation, maximum vertical axis rotations increase progressively from the apex to both arc limbs (Figures 4, 6, and 8).

In all models the silicone pierces the surface at the end of the experiment. It occurs as elongated up-welling silicone bodies known as silicone walls at the arc tips and as silicone tongue canopies at the apex part (Jackson et al., 1986). These silicone canopies are sometimes added to the fold-and-thrust belts as deformation proceeds.

10.1029/2021TC006955

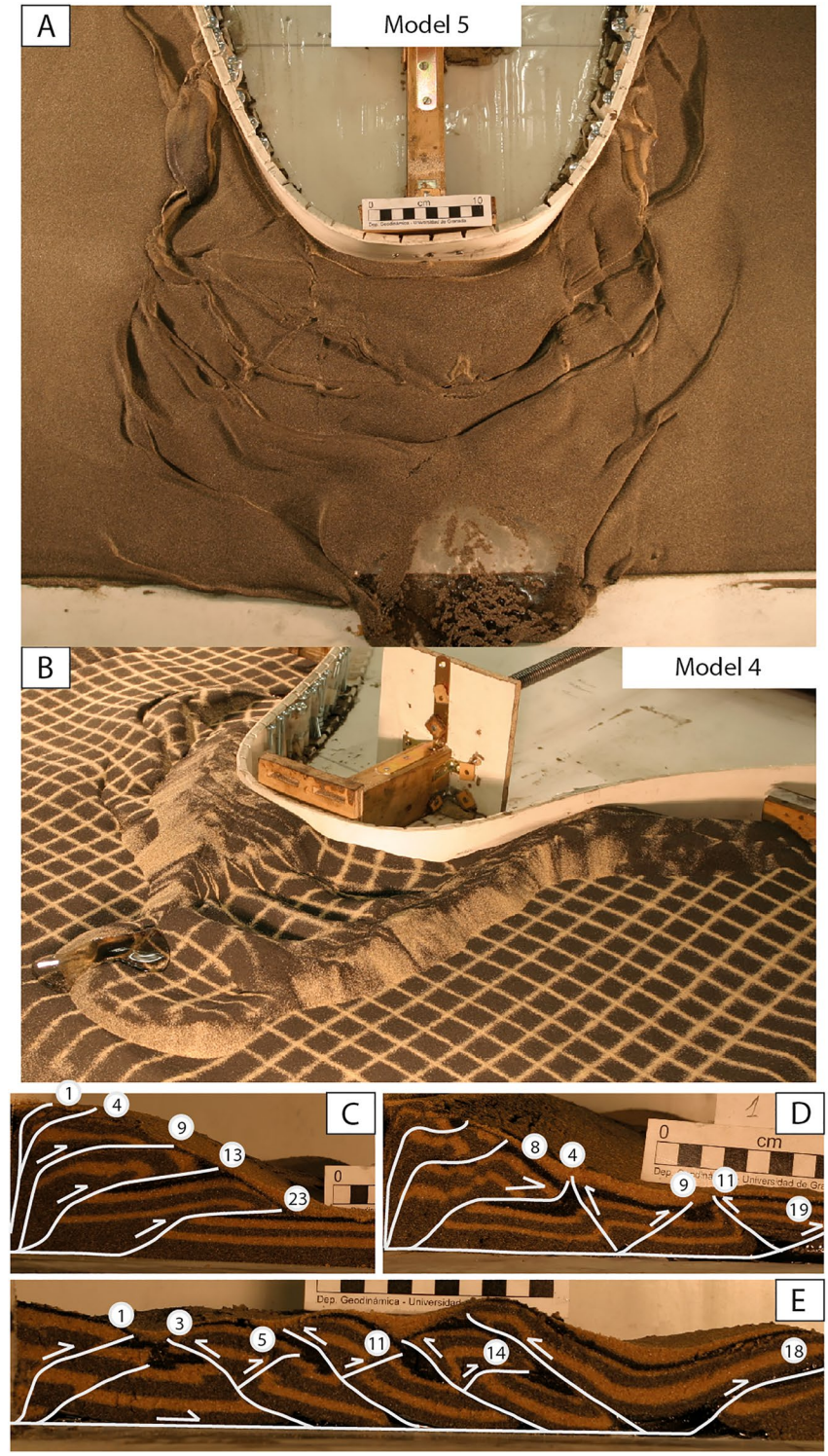

Figure 7. Photographs of Models 4 and 5. (a) Silicone topography of Model 5 (b) Oblique picture of Model 4. (c–e) cross-sections of subparallel to the transport direction of Model 4. See Figure 6a for cross-section locations. All pictures were taken at the end of the experiments.

In the next sections, we will highlight the target features developed in each model group. For comparison purpose, the deformation sequence is shown in four stages (S1 to S4), being the apex displacement for each stage coincident with that of the equivalent stage shown in Figures 4, 6, and 8 of Jiménez-Bonilla et al. (2020). The

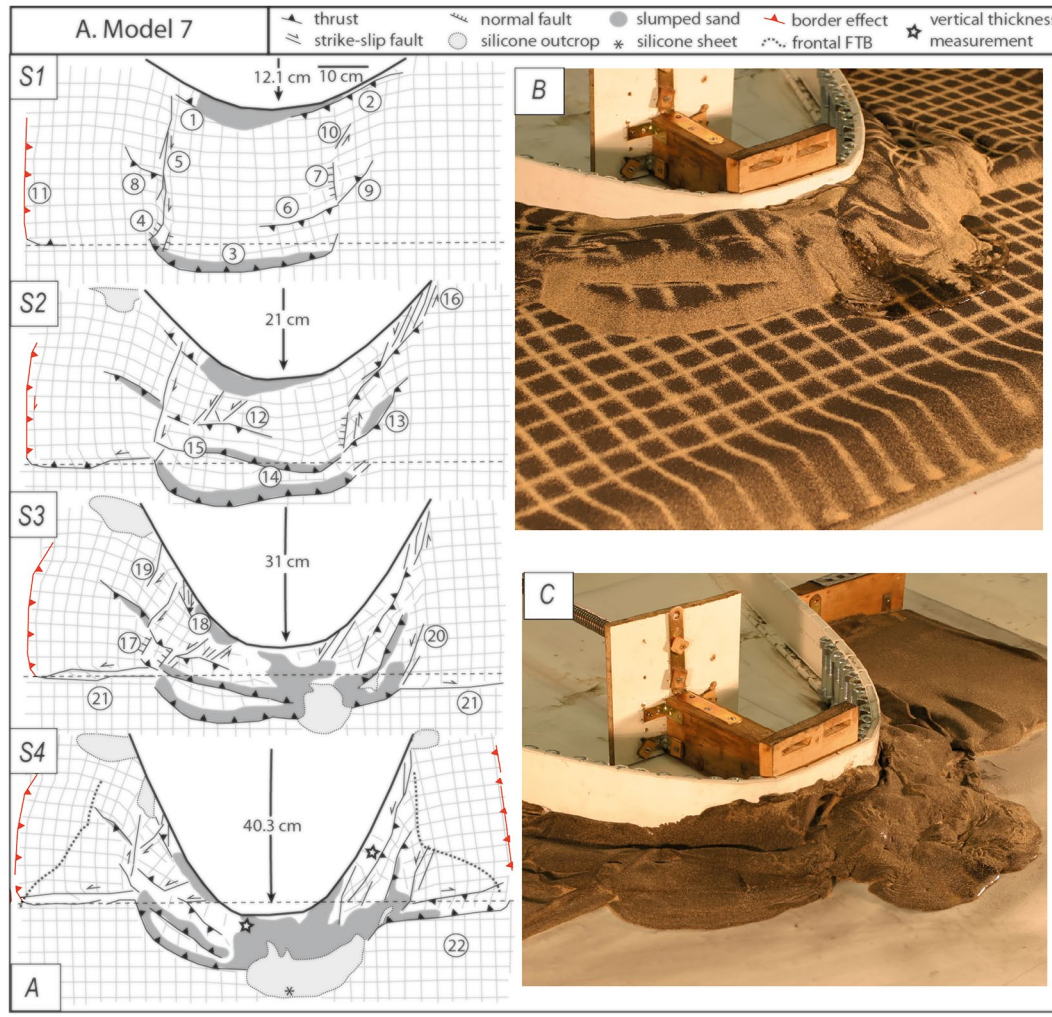

Figure 8. (a) Line drawings of the stages S1–S4 of Model 7 that includes a frontal silicone pinch-out –marked by dashed line-. The numbering indicates the relative chronology of structures. The apex displacement is indicated for each stage. Structures related to border effect are in red. Dotted line shows the deformation front. (b) Oblique picture of the resulting fold-and-thrust belt of Model 7 (c) Oblique picture of the silicone topography at the end of the Model 7.

chronology of structures is indicated by numbering. Border effect structures in the lateral and frontal boundaries of the analog pack have not been drawn (except for Models 6 and 7, see below). The videos of the experiments are included as Videos 1 to 7 that coincide with Models 1 to 7.

3.1. Models With Pre-Deformational Diapirs (Models 1–3)

Both Figure 2 and S1 in Figure 4 shows the diapirs size and distribution for each model. All these models were shortened between 35 and 42 cm in the apex.

3.1.1. Deformation Sequence

At the first stage (S1; Figure 4), most structures, including fold-and-thrust belt fronts were highly conditioned by the location of diapirs. Thrusts, normal and strike-slip faults nucleated surrounding diapirs or linking them by means of strike-slip faults. Differences of displacement between thrust segments are accommodated by transfer zones (i.e., fault 5 in Model 1; fault 2 in Model 3; Figures 4a and 4c). In the three models, the vertical thickness in the internal parts of the fold-and-thrust belts roughly doubled the original one (Table 2).

As deformation proceeded (S2; Figure 4), fold-and-thrust belts thickened significantly but widened only slightly. Arc-parallel stretching was mostly accommodated by normal faulting in Model 2 (faults 12; Figure 4b) whereas

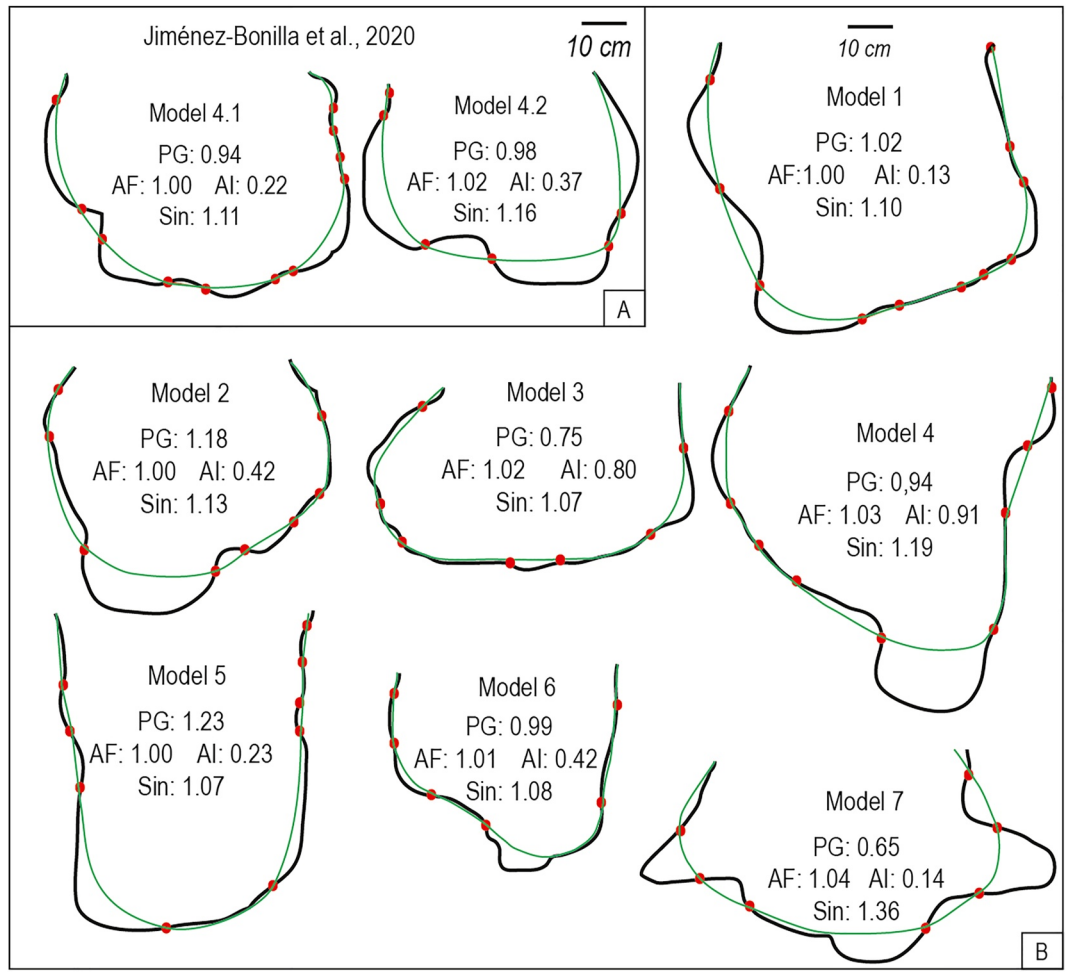

Figure 9. (a) Frontal thrust line drawing, Sin calculations and results of Protrusion grade, Asymmetry factor, AL for Models 4.1 and 4.2 (Jiménez-Bonilla et al., 2020) (b) Idem for our Models 1 to 7.

strike-slip faulting was more pervasive in Model 1 (faults 12; Figure 4a). In Model 3, strike-slip faults were mostly generated in the left arc limb, with diapirs (e.g., fault 7; Figure 4c) whilst normal faults were more frequent in the right arc limb (e.g., faults 8; Figures 4c, 5a, and 5b). Geometric indexes show that Models 1 and 2 developed symmetrically and protruded at the late stages (Figures 4, 5a, 5b, and 9b and Figure S1). Although Model 3 nucleated really asymmetric due to the original diapirs distribution, it evolved into a more symmetric fold-and-thrust belt at S4 (Figure 4c and Figure S1).

During the last deformation stages (S3 and S4; Figure 4), short new thrusts were generated, which allowed the fold-and-thrust belt protrusion grade (PG) to increase in Models 1 and 2, although they did not accommodate much displacements (e.g., thrusts 16, 17, 18 and 19 in Figures 4a and 5). Instead, shortening was mostly accommodated by both tightening of previous structures, such as pop-up and pop-down structures, and overlapping increase of previously formed hanging wall sheets (Figures 5d and 5e, respectively). Tightening of previous structures made vertical thickness to increase up to 8 cm at the end of the experiment (400%) in Model 3 (Table 2 and Figure 4c). Moreover, slumped sand was mixed with silicone deposited on thrust footwalls, especially in the apex part of Models 1 and 3 (α up to 35°; Table 2 and Figure 4). The highest overlapping is frequently found in thrusts and backthrusts nucleated in relation to diapirs (e.g., thrust 8; Figures 4a and 5e). Some of these structures could have acted either as active or passive roof thrusts such as backthrust 16 of Model 1, which covered pro-verging thrusts 1 and 8 (Figure 4a; Couzens-Schultz et al., 2003). Although all diapirs were incorporated into the fold-and-thrust wedge, those located at the most external part were less deformed and can be easily distinguished in the silicone topography (Figure 5b). Finally, it is worth mentioning the important role of normal faults

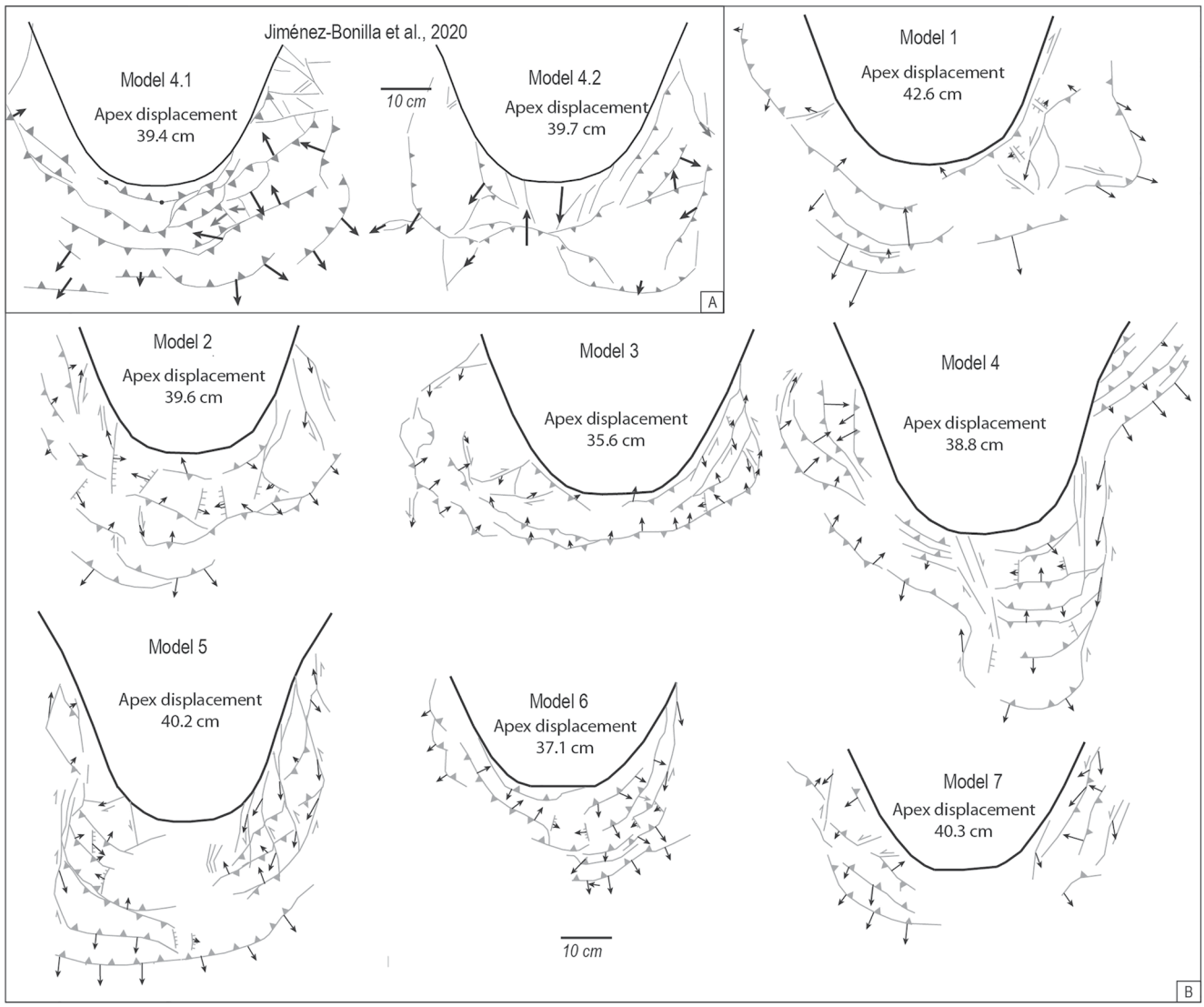

Figure 10. (a) Displacement vectors for Models 4.1 and 4.2 (Jiménez-Bonilla et al., 2020) (b) Idem for Models 1 to 7.

on the along-strike segmentation of fold-and-thrust belts at the end of experiments (Figures 4, 5a, and 5c). In Model 3, maximum vertical axis rotations occurred in the limb without diapirs (55° vs. 40° in the diapirs-bearing limb; Figure 4c).

3.1.2. Fold-and-Thrust Belt Geometry and Kinematics

At the end of the experiments, we distinguished significant differences in the plan view geometry of the resulting fold-and-thrust belts. Models 1 and 2 show higher protrusion (PG > 1) than Model 3 (PG < 1) (Figure 9b and Table 1). These three models are roughly symmetric (AF is ca. 1), but Model 3 seems to be slightly less symmetric (lower AI value) than the others (Figures 4 and 9b and Table 1), due to the development of two salients in the lateral parts of the arc. The salient located in the left arc limb with diapirs is bigger than that one in the arc limb without diapirs (Figure 9b and Table 1). Despite the presence of these big salients in Model 3, the fold-and-thrust belt sinuosity is similar in Models 1 to 3 (Sin ca 1.1 in Models 1 to 3. Figure 9b and Table 1). Although shortening is higher in the apex part than in the lateral parts, fold-and-thrust belts are never wider in segments in front of the indenter apex (e.g., 20 cm wide in Model 3 is achieved between the apex and lateral parts; Table 1). Thus, the deformation in the apex does not propagate toward frontal parts, but is mostly accommodated by vertical thickening, which largely surpass 250% (Table 2). This thickening is particularly significant in model 3 where it is coupled with the highest variation of α (35° in the apex to 5.7° in the lateral parts, Table 2). Some fold-and-thrust

belt segments in Models 1 and 3 reached their supercritical angle as pointed out by the presence of gravitational deposits. Conversely, Model 2 shows an along-strike constant α below the critical value.

Transport directions define an almost radial outwards pattern in every model and all the structures at the arc limbs are oblique faults, as deduced from their angular relationships with the associated kinematic vectors (Figure 10b). The maximum fan angle defined by thrust kinematic vectors is significantly larger in the model with big silicone diapirs (Model 1) (Figure 10b). Most kinematic vectors do not vary significantly along structures, thus transpression occurred at the lateral parts of thrusts (e.g., thrust at the right of Model 1; Figure 10b). Some early thrusts especially those nucleated at the arc limbs, rotated while their kinematic vectors maintained their orientation, thus evolving into transpressive bands (e.g., thrust 5 and 11 in Figures 4c and 5a). In the left, diapirs-bearing limb of Model 3, pervasive strike-slip faults developed oblique to the indenter strike, and shortening was mainly accommodated by thrusts and backthrusts. By contrast, transpressive bands were formed subparallel to the indenter in its right arc limb (Figures 4c, 5a, 5b, and 10b).

3.2. Models With Silicone Bands Parallel to the Apex Movement (Models 4–6)

This section deals with those experiments that include silicone bands of different thickness oriented parallel to the apex movement (Models 4 to 6). The boundaries between bands are represented with dashed lines (Figure 2 and S1 in Figure 6 and Table 2; see also Section 2.3). Note that dashed lines in Model 4 correspond to silicone pinch-outs. In Model 6, remarkable border effects developed as thrusts surrounding the whole external boundary of the analog pack. These structures are excluded for further analyses (structures in red in Figure 6c). All these models were shortened at the apex part between 37 and 40 cm.

3.2.1. Deformation Sequence

At the early stages (S1), both thrusts and backthrusts were nucleated where silicone was present (e.g., thrusts 1 in Figures 6a–6c), whereas only thrusts formed at silicone-free areas of Model 4 (Figure 6a). Normal faults are localized in Model 4 related to the silicone pinch outs (e.g., fault 5 in Figure 6a). Strike-slip faults concentrated at the arc lateral zones in all models whether silicone is present or not (e.g., fault 2 in Figure 6a, faults 4 and 5 in Figure 6b, faults 6 and 7 in Figure 6c). Despite silicone sheet variations, no protruded lobes in plan view were generated at such low shortening values and PG was less than 0.7 (Figure 9b). Differences in the detachment layer between both arc branches in Models 4 and 6 produced lateral lobes and thus AI > 1 (Figure 9b).

As deformation proceeded (S2), different fold-and-thrust belt segments started to be individualized. Foreland-verging, closely spaced thrusts were formed in fold-and-thrust belt segments detached either within sand or 0.2-cm-thick silicone sheets (see Model 4 and the right part of Model 6; Figures 6 and 7b). These wedges were significantly thicker than those formed over silicone sheets thicker than 0.3 cm, where pop-up and pop-down structures dominated (Figures 6, 7d, and 7e). Differences on the displacement between these segments were accommodated by fault zones composed of oblique, normal and strike-slip faults, which acted as transfer zones (e.g., normal faults 12 in Figure 6a and strike-slip faults 11 in Figures 6c, 7a, and 7b). These relay zones were frequently localized in relation to boundaries between different silicone thickness bands.

In the third deformation stage (S3), those fold-and-thrust belt segments floored by thick silicone layers propagated toward the front, drawing prominent salients in plan view (see thrusts 18 and 17 in Models 4 and 5, respectively; Figures 6a and 6b). However, the fold-and-thrust belt width in Model 6 is not sensitive to the indenter advance. In its left limb, the back-thrust 14, detached within a thicker silicone sheet, acted as a roof fault covering a pop-up formed by thrusts 4 and 5 (Figure 6c). This passive roof thrust accommodated nearly all the shortening in this arc limb (Figure 6c). In the right limb, an pro-verging imbricate system developed along with scarce back-thrusting (Figure 6c). Different displacements between fold-and-thrust belt segments produced large transfer zones (e.g., fault zone 20; Figure 6b). These fault zones maintained their strike in spite of the change of the indenter shape, thus changing their kinematics.

During the last stage (S4; Figure 6), new thrusts nucleated and frontal thrusts propagated toward more external parts, especially in the apex part, so the wedge protrusion increased significantly (Figures 6 and 9b). The PG actually increased from S1 to S4 in Models 4 to 6 (Figure S1). This protrusion is always favored by the thicker silicone layers. Although both salient and recesses formed in plan view, fold-and-thrust belts developed roughly symmetric: AF values remained constant and AI values even decreased from S1 to S4 in Models 5 and

6 (Figure S1). Silicone canopies covered part of the fold-and-thrust belts at the apex part, but also at the arc tips (Figures 6a and 6b). The maximum vertical axis rotations occurs over the thicker detachment layer in the three models, reaching 65° in the left branch of Model 4, and 55° in models 5 and 6 (Figure 6).

3.2.2. Fold-and-Thrust Belt Geometry and Kinematics

These models show highly protruded fold-and-thrust belts with big lobes (Figure 9b and Figure S1). The geometry (protrusion, sinuosity and asymmetry) of the resulting fold-and-thrust belts are highly influenced by the location, thickness and geometry of the silicone layer: the salient chord length is always related to the layer width (Figure 9b and Table 1). Recesses are often related to transfer zones (Figure 6).

In Model 5, the underlain silicone band is located in front of the indenter apex, provoking a higher protrusion (PG > 1) than in Models 4 and 6 (PG < 1), where the presence of alternating silicone generates salient and recesses (Figures 6 and 9b). Although Models 4 and 6 are asymmetric due to the geometry of their salients, AF is not sensitive to them and maintained at ca. 1 from S1 to S4 (Figure 9b). However, AI does show distinctive values in Models 4 to 6, thus accounting for obvious symmetry differences (Figure 9b and Table 1). Conspicuous salient and recesses developed in Model 4, which includes silicone pinch-outs, resulting in a high Sin. In contrast, models 5 and 6, which do not contain silicone pinch-outs, show low sinuosity (Sin < 1.1).

The maximum vertical thickness corresponds to the fold-and-thrust belt segment detached within sand in the apex part of Model 4 (Table 2 and Figure 7b). Interestingly, for the same silicone thickness, maximum vertical thickening and α are frequently higher at the arc limbs than in the apex, although shortening is higher in the apex (See Models 4 and 6; Figures 7d and 7e; Table 2). This is because in the lateral parts, strain localized in the most internal fold-and-thrust belt whilst it was more distributed in the apex part where fold-and-thrust belts are always wider (Figures 7d and 7e). In Model 6, α is higher in the fold-and-thrust belt detached within the thicker silicone sheet due to the presence of a backthrust that covered a pop-up structure (Figure 6c).

Kinematic vectors associated with thrusts change gradually along fold-and-thrust belts of all models, even in faults constrained to one single silicone band. Maximum angles between kinematic vectors associated with pro-verging thrusts were around 90° in Models 4 and 5, and significantly larger in Model 6 (Figure 10b). Arc-parallel stretching is accommodated either by normal fault zones perpendicular to the indenter strike (e.g., in Figure 10b) or by transfer zones, which are mainly composed of oblique faults (Figure 6c). It is worth noting that scarce normal faults develop in Model 4, thus arc-parallel stretching is mainly accommodated within strike-slip dominated transfer zones (Figures 6c and 10b). As in models 1 to 3, vertical axis rotations of previous structures resulted in changes in their kinematic regimes. Thus, most thrusts located at the arc limbs eventually evolved into transpressive bands (e.g., right side of the Model 6; Figure 6c).

3.3. Model With a Frontal Silicone Pinch-Out (Model 7)

Model 7 shows the effect of a frontal pinch-out, which is shown by a dashed line in Figure 8a. The deformation front is drawn by linking the thrust related to the silicone pinch-out to the arc tips. Structures due to border effects such as thrust 11 are drawn in red (Figure 8a). The deformation front at the lateral parts has been drawn linking the tips of faults 21 and 22 with the arc tips. The strain partitioning mode is similar to that of previous Models 1 to 6 until the frontal thrust reaches the silicone pinch-out, which conditions the later propagation of the deformation.

3.3.1. Deformation Sequence

At S1, the main structure to nucleate in Model 7 was a frontal thrust originated at the frontal silicone pinch-out (thrust 3, Figure 8a). This frontal thrust was linked to the indenter at both tips with long transfer zones composed of normal faults (e.g., fault 7) and strike-slip faults (e.g., fault 5; Figure 8a). Thus, a protruded and symmetric fold-and-thrust belt formed, hosting a relatively undeformed block at its inner part (Figures 8 and 9b and Figure S1).

At S2, the frontal thrust 3 slowly moved forward as the central block thickened due to the formation of new thrusts and backthrusts (Faults 13, 14, and 15; Figure 8a). A transpressive band nucleated at the most internal part of the right arc limb (Fault 16), whilst conjugate strike-slip faults favored the formation of a salient in the left arc limb, increasing the overall asymmetry (Figures 8a and 9b and Figure S1). Significant vertical axis rotations up to 30° occurred at both arc limbs.

As deformation proceeded (S3), no new thrusts were formed, the main thrust 3 slowed down its advance toward the front and shortening was mostly accommodated by vertical thickening of the wedge. Arc-parallel stretching was accommodated by new normal faults subperpendicular to the indenter strike (Fault 17; Figure 8a). Wedge reached its supercritical angle at the apex part, therefore sand started to slump and silicone pierced the surface, mixing both at the fold-and-thrust belt toe. At the same time, lateral extrusion is observed along faults 21 (Figure 8a).

In S4, the frontal thrust propagates to the lateral parts of the arc (thrust 22), closely following the silicone pinch-out. Other fold-and-thrust belt segments reached the supercritical angle and outcrops of slumped sand and silicone extended toward the arc limbs. These gravitational deposits covered previous structures as canopies at the most frontal part (Figures 8a–8c). Because of fold-and-thrust belt frontal stagnation, the wedge protrusion diminished progressively (Figure 9b and Figure S1). Model 7 always shows a quite symmetric fold-and-thrust belt, AI even decreased from S1 to S4 (AF ca. 1 and AI decreased from ca. 0.5 up to ca. 0.2; Figure 8a and Figure S1). Maximum vertical axis rotations reached 50° at the arc limbs.

3.3.2. Fold-and-Thrust Belt Geometry and Kinematics

The resulting fold-and-thrust belt shows both low protrusion grade and a relative narrow frontal fold-and-thrust belt because deformation did not propagate outwards during the last stages (Figures 8a and 10b, Table 1). Moreover, two big lateral salients developed behind the pinch out, thus increasing sinuosity whereas symmetry is not affected ((Sin reached 1.36 whilst AF and AI values at S4 were low; Figures 8a and 9b, Table 1). The resulting fold-and-thrust belt at the arc limbs is composed of pop-up and pop-down structures, whilst the frontal fold-and-thrust belt is covered by gravitational deposits made up of slumped sand mixed with silicone, which were eventually added to the belt. The highest vertical thickening, of around 500%, is reached in the apical part along with the larger α, both decreasing toward the arc limbs (Table 2). The maximum angle between kinematic vectors associated with thrusts was 75° (Figure 10b). In this model, a transpressive band formed only at the right side, whilst dip-slip dominated thrusts formed at the left side (Figure 10b).

4. Discussion

The experiments presented here used a flexible indenter that deformed in map view while the experiment progressed: the indenter geometry changed from nearly straight (PG ca. 0; Figures 1c and 2) to arcuate (PG 0.65 at S4; Figure 1c) to reproduce the evolution of curved fold-and-thrust belts in progressive arcs. Previous experiments of curved fold-and-thrust belts that used a rigid backstop did not modeled typical features of progressive arcs such as strongly divergent thrust (variations > 100°), severe arc-parallel stretching or vertical axis rotations higher than 25° at the arc limbs (See Table 3 in Jiménez-Bonilla et al., 2020). Our models were designed under two main premises: (a) they are developed as progressive arcs, and (b) the viscous layer where the main detachment localizes presents different geometrical heterogeneities, such as diapirs, lateral thickness variations and pinch-outs (Figures 1–10). This permits to compare our new progressive arc models with previous experiments (piedmonts models and protruding backstop models), which do not include heterogeneities at the base, as well as with natural cases.

Piedmont experiments, which are gravity driven models, reproduced outward transport directions and arc-parallel extension both in models composed only of silicone and models composed of sand and silicone (Driehaus et al., 2013; Gautier et al., 1999; Gilbert & Merle, 1987; Jiménez-Bonilla, Crespo-Blanc, et al., 2017). Although the frontalmost parts of piedmont experiments registered shortening, that is, rolling zone, no real fold-and-thrust belts built up. Indeed, arc-perpendicular extension developed at the rear of piedmont arcs. Another significant difference is that PG of the outer arc is lower than 0.4 in all piedmont models whereas it is always higher than 0.65 in progressive arcs generated by a protruding backstop (Jiménez-Bonilla, Crespo-Blanc, et al., 2017; Figure 9).

Irrespective of their differences on the initial detachment geometry and thickness, experiments that use a protruding indenter generate fold-and-thrust belts that share several characteristics (Jiménez-Bonilla et al., 2020; Crespo-Blanc et al., 2017; Jiménez-Bonilla et al., 2018, 2020; Figures 3–10). In these models, PG is higher than 0.65, transport directions are radial and the maximum angles between kinematic vectors associated with thrusts are higher than 75° (Figure 10). Outwards transport directions provoke significant arc-parallel stretching often accommodated by distributed normal and strike-slip faults, especially when heterogeneities in the viscous layer are present (Models 1 to 7; Figures 4–10).

The presence of different detachment heterogeneities in our Models 1 to 7 strongly control both the strain partitioning modes and the strain localization in progressive arcs (Figures 4–10 vs. Models 4.1 and 4.2 in Jiménez-Bonilla et al., 2020, Tables 1 and 2). In Section 4.1 we will analyze the wedge geometry obtained in our models and compare it with previous ones. In Sections 4.2–4.4 we will delve into the strain localization and partitioning of the different experiments (with diapirs, viscous layer thickness variations or pinch-outs), and their applicability to natural progressive arcs.

4.1. Controls on Wedge Geometry: Protruding Versus Rigid Indenters

Previous works that used a rigid backstop pointed out that homogeneous detachments, either frictional or viscous, favor self-similar vertical and horizontal growth with the taper angle remaining constant during the whole experiment and along the fold-and-thrust belt (Davis et al., 1983). In the same way, the wedge taper angle seems to be constant in experiments that use a protruding backstop (Jiménez-Bonilla et al., 2020). Conversely, any heterogeneity in the viscous detachment layer, whether diapirs, pinch-outs or variations in the detachment layer thickness, generates variations on α during the experiment and along the fold-and-thrust belt trend (Models 1 to 7; Figures 4–10).

Heterogeneities along the transport direction, regardless of whether they are produced by diapirs or viscous layer pinch-out, seem to act similarly: the deformation front stagnates upon reaching the heterogeneity and, then, wedges increase their taper angle, especially at the external fold-and-thrust belt (Costa & Vendeville, 2002; Li & Mitra, 2017; Crespo Blanc & Gálvez, 2008; Crespo Blanc & Gálvez, 2008; Models 1, 2, 3 and 7; Figures 4 and 8 and Table 2). However, experiments that use a rigid indenter do not seem to reach the supercritical angle, as our models do, since they do not generate gravitational bodies such as slumps sand deposits (Crespo Blanc & Gálvez, 2008; Duffy et al., 2018, 2020; Sans, 2003).

The presence of a higher α and the deposition of gravitational deposits in our models could be related to the development of either transpressive bands (models 1, 2, 3) or a highly dipping, frontal monocline (Model 7). Transpressive bands develop because most kinematics vectors are oblique to thrusts (Figure 10b). Transpression is often associated with high vertical growth and related higher α values, as it occurs in our models (Figures 4–10 and Table 2).

In our Model 7, as well as previous experiments with similar basal heterogeneity, shortening is accommodated by a continuous pop-up structure (Bahroudi & Koyi, 2003; Nilforoushan & Koyi, 2007; Li & Mitra, 2017; Model 7, Figure 8). By contrast, fold-and-thrust belts sharply interrupted along strike are generated in experiments with diapirs (Crespo Blanc & Gálvez, 2008; Models 1 and 2; Figures 4 and 9).

Irrespective of the backstop type (protruding or rigid), variations of the detachment layer along the fold-and-thrust belt trend provoke differences on α along this direction: α is higher in fold-and-thrust belt segments detached within frictional detachments or those presenting diapirs (e.g., Bahroudi & Koyi, 2003; Models with a protruding backstop; Models 3, 4, 5, and 6; Figures 4 and 6; Table 2).

Also, regardless of the backstop type, the presence of silicone bands with variable thickness arranged parallel to the indenter movement results in fold-and-thrust belts with salient and recesses in plan view (Figures 4, 6, and 8; See values of AF, AI and Sin values in Table 1; Koyi and Cotton, 2000; Bahroudi & Koyi, 2003; Koyi & Sans, 2006; Nilforoushan and Hemin, 2007; Li & Mitra, 2017). Fold-and-thrust belt segments detached within sand or thin bands of silicone are narrow and characterized by piggy-back imbricates whose α remains constant: new forethrusts are added as vertical thickening occurs at the internal parts (Table 2). Thicker viscous substrates generate wide fold-and-thrust belt segments characterized by box folds and lower α angles, which increase during time (Table 2). Transfer zones, accommodating the differential salient-recess displacement, also seem to be mainly related to basal heterogeneities rather than the backstop type. However, a significant arc-parallel stretching is inherent in our progressive arc models because of the gradual change of the indenter geometry that provokes radial outwards transport directions. This arc-parallel stretching is often accommodated within transfer zones, and they exhibit a high degree of strain partitioning among normal, strike-slip and oblique-slip faults. In contrast, transfer zones in previous experiments with non-deformable backstops systematically consist of pure strike-slip fault zones, nearly parallel to the thrusting direction (Figures 1, 6, and 10b vs. Bahroudi & Koyi, 2003). Moreover, transfer zones maintain their strike in our progressive arc models, so their overall kinematic regime changes.

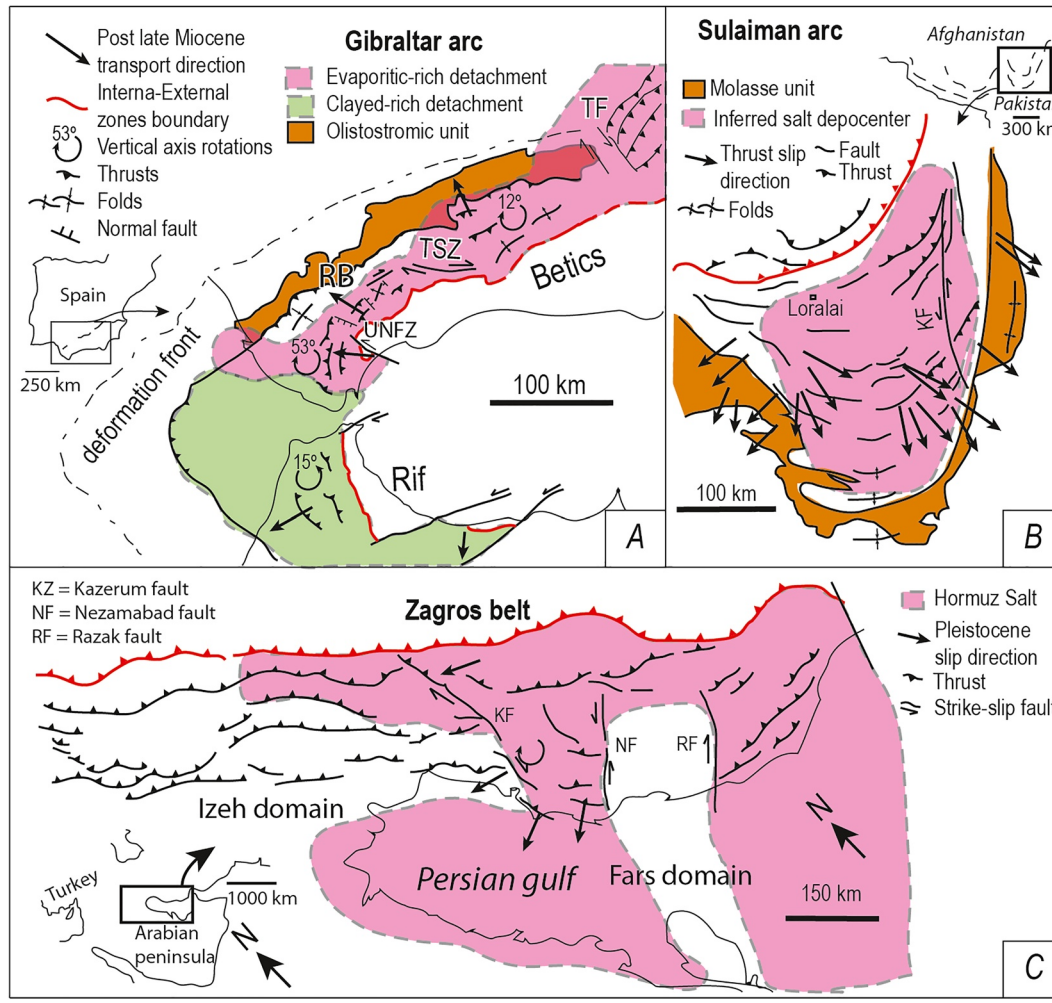

Figure 11. (a) Simplified structural map of the Gibraltar Arc with structural trend, vertical axis rotations and kinematic vectors (Crespo-Blanc et al., 2016). UNFZ: Ubrique Normal Fault Zon; RB: Ronda Basin, TSZ: Torcal Shear Zone, TF: Tiscar Fault, (b) Structural map of the Sulaiman. KF: Kingri Fault (Jadoon et al., 1994, 2020; Lillie, 1991; Reynolds et al., 2015) and (c) Zagros belt (Bahroudi & Koyi, 2003; Letouzey et al., 1995; McQuarrie, 2004).

4.2. Strain Localization at Diapirs

Previous analog models pointed out that the presence of diapirs promotes the nucleation of structures that usually link them (Crespo Blanc & Gálvez, 2008; Duffy et al., 2018, 2020; Roca et al., 2006; Rowan & Vendeville, 2006). In our models 1 to 3 diapirs seem to block the wedge propagation as observed in Section 4.1. Normal faults, which accommodate arc-parallel stretching, are localized close to diapirs (Figures 4 and 5).

Some natural cases of progressive arcs show significant along-strike segmentation. For instance, the northern branch of the Gibraltar arc fold-and-thrust belt, that is, the Betics, is mostly underlain by $a > 0.2$ km thick viscous layer of Triassic evaporites (e.g., Vera, 2004). Pre-deformational diapirs have been observed in areas with moderate bulk shortening in the lateral parts of this arc (Martínez del Olmo et al., 2015; Nieto et al., 1992; Rubinat et al., 2013). Such diapirs are expected all along the betic fold-and-thrust belt (Berastegui et al., 1998; Nieto et al., 1992), although they are hardly identified probably due to complex structures formed by higher shortening in the apical part of the Gibraltar arc. Such pre-deformational diapirs might have played a key role on the nucleation and development of normal and strike-slip fault zones along the Betic fold-and-thrust belt strike for example, Balanyá et al., 2007; Jiménez-Bonilla, Expósito, et al., 2017) as observed in our Models 1 to 3 (Figures 1, 4, and 11a). In this regard, traverse faults along the Betics are related to the widespread Triassic evaporites, which could be associated with pre-deformational diapirs, that influenced the localization of major fault

zones, such as the Ubrique Normal Fault Zone (UNFZ), the Ronda Basin normal faults or the Tíscar Fault Zone (Jiménez-Bonilla et al., 2015, Jiménez-Bonilla, Expósito, et al., 2017; Sanz de Galdeano et al., 2006; Figure 11a). Thus, the localization of extension associated with pre-deformational diapirs could be responsible for the development of intermontane basins along the Betics such as the Ronda basin (Figure 11a).

4.3. Lateral Variations of the Detachment Layer: Controls on Strain Partitioning and Protrusion Grade

Previous analog (Bahroudi & Koyi, 2003; McQuarrie, 2004) and numerical (Ruh et al., 2012, 2017) models of the Zagros fold-and-thrust belt have tested the influence of lateral variations in the rheology of the basal detachment layer, including a viscous layer pinch-out parallel to the indenter displacement. In a similar way, our Model 4 alternates viscous and frictional bands, producing three pinch-outs parallel to the indenter displacement. Thus, in the right half of the model, the viscous detachment is located in the apex and the frictional one is in the lateral part of the arc, whereas the disposition is the opposite in the left half of the arc (Model 4; Figure 6a).

The right half of our model produces similar results to such previous models of Bahroudi and Koyi (2003), which used a rigid indenter to model the Zagros. Thus, irrespective of the indenter behavior, the belt over the viscous detachment is significantly wider and exhibit lower taper angles than that developed over the frictional one (Figures 6 and 7). Although there are not evidences of a protruding indenter in the Zagros belt, these features resemble, for example, those observed between the Fars domain (SE Zagros Simply Folded Zone), detached at the viscous Hormuz Salt (Letouzey et al., 1995) and the Izeh domain (NW Zagros Simply Folded Zone), mostly detached at frictional shales (McQuarrie, 2004, Figure 11c).

As discussed in Section 4.1, a consequence of width differences along fold-and-thrust belts is that wider segments over viscous detachment typically produce arc salients, thus increasing the sinuosity of the arc front in map view. These salients are connected to the narrower segments by strike-slip dominated or transpressional transfer zones localized at the viscous pinch-out (fault 2 in our model 4, Figure 6a: compare with domains D and E of Bahroudi & Koyi, 2003, in their Figure 4). This transfer zones would likely be represented in the Zagros fold-and-thrust belt by the Kazerum and associated faults (Bahroudi & Koyi, 2003, Figure 11c).

In contrast to the right side, in the left side of our Model 4, both apex and lateral segments present similar widths and taper angles (Figure 6a). In this case, the segment with the viscous detachment is located at the lateral part of the arc, where the orthogonal shortening for a certain amount of total indenter displacement is significantly lower than in the apical part. Consequently, sinuosity does not increase and no transfer zones are formed at the viscous pinch-out.

Although the above-mentioned experiments (Bahroudi & Koyi, 2003; McQuarrie, 2004) reproduce certain features of the Zagros, they neither reproduce the angle between transport directions, up to 60°, nor the vertical axis rotations observed along the fold-and-thrust belt in the Fars domain (Hatzfeld & Molnar, 2010; Hessami, 2002, Figure 11c). Indeed, regardless of the indenter geometry, the path and/or the viscous detachment layer geometry, the maximum angle between kinematic vectors is always lower than 25° in experiments with rigid indenters (Crespo Blanc & González Sánchez, 2005, Figure 10). Consequently, our results suggest that the Fars domain probably behaved as a progressive arc with viscous detachment pinch-outs parallel to the indenter movement (Model 4; Figures 6a and 11c). Additionally, as in the Zagros, normal faults accommodating arc-parallel stretching are scarce, out of transfer zones, in our Model 4. The lack of normal faults in the Zagros would be explained by the accommodation of arc-parallel stretching within transfer zones such as the Kazerum and Nezamabad fault zones (Hatzfeld &Molner, 2010, Figure 11c). This agrees with episodes of Cenozoic transtension that have been observed in the Kazerum fault zone (Sepehr & Cosgrove, 2005).

Our models 5 and 6 suggests that differences in width (contributing to the arc sinuosity), relief and structural style along belts are not only related to viscous versus frictional detachments. They can also be produced above viscous detachments if the viscous layer presents significant lateral thickness variations (Figures 6b and 6c; Tables 1 and 2). The boundary between the thicker and thinner segments acts similarly to a viscous pinch-out, localizing narrow, transfer zones that accommodate the differential frontal propagation of the salients generated at the thicker viscous layer segments. However, the presence of silicone pinch-outs, either parallel or perpendicular to the apex movement (models 4 and 7, respectively), favored higher differences in frontal propagation along the fold-and-thrust belt, thus increasing their mountain front sinuosity (See values of Sin of models 4 and 7 in Figure 9b).

In our Model 5, the thicker silicone band located in the apex part favors the development of a strongly protruded arc (PG = 1.23; Figures 4 and 9b). The Sulaiman arc, which seems to work as a progressive arc (Lillie, 1991; see Figure 4d in Reynolds et al., 2015), is underlain by a 1.2 km thick Precambrian salt layer that decreases up to 0.3 km to the arc limbs (Jadoon et al., 1994, 2020; Figure 11b). This layer acts as a ductile layer and its pre-deformational thickness variation seem to have conditioned the high PG of this arc. Moreover, the transfer faults that limit the arc salient could be associated with pinch-outs or strong thickness variation of the salt layer (Jadoon et al., 1994, 2020). In the same way, the pre-orogenic Triassic evaporite-rich layer localizing the detachment in the northern branch of the Gibraltar Arc is likely thicker than 1 km in the apex part, decreasing toward the arc limb (Vera, 2004; Jiménez-Bonilla et al., 2016, Figure 11a). This thickness variation could have conditioned the wide fold-and-thrust belt developed at the apex, the strongly protruded plan view geometry of the Gibraltar Arc fold-and-thrust belt (PG > 1.3 using the deformation front trace) and the development of the narrow, transpressional Torcal shear zone at the northern lateral segment (Barcos et al., 2015, Figure 11a).

Differences of vertical axis-rotations have been observed between both arc limbs in some natural cases of progressive arcs. In the Gibraltar arc, the maximum vertical axis rotations during the late Miocene are 53° clockwise and 15° counterclockwise in its northern and southern branches, respectively (Crespo-Blanc et al., 2016, Figure 11a). In the Northern Apennine arc, its northern branch rotates 40° whilst 15° its southern one (Turtù et al., 2013). Our Model 6 suggests that these differences in vertical-axis rotations could stem from either variations in the viscous layer thickness between both arc branches (Model 6; Figure 6c) or lateral pinch-outs, which produce a similar effect, as discussed above. Indeed, the detachment in the Gibraltar arc is related to an evaporitic-rich layer in its northern branch (Vera, 2004), while it is a more clayed layer in the southern one (Chalouan et al., 2008). In a similar way, in the Northern Apennine arc the detachment is localized on a Messinian clayed-rich formation in its northern branch while in its southern one is made up of limestones (Turtù et al., 2013).

4.4. Frontal Viscous Layer Pinch-Outs

As we described in Section 4.1, the frontal silicone pinch-out of our Model 7 produced frontal stagnation and wedge thickening until reaching its supercritical angle (Figure 8). This fact led to large gravitational deposits localized by the pinch-out. This analog model allows us to better understand the Central Betics fold-and-thrust belt, where the evaporitic-rich layer displays a pinch-out oriented ca. N75°E, which is perpendicular to the thrusting transport direction at this segment (Jiménez-Bonilla et al., 2016). Previous works have suggested that this pinch-out could be the main cause for the deformation front stagnation and the subsequent taper angle increase (taper angle > 10°), which promoted the deposition of a gravitational olistostromic unit during the middle Miocene (Jiménez-Bonilla et al., 2016; Roldán et al., 2012). In addition to a silicone pinch-out perpendicular to the apex movement, our models 1 to 3 also suggest that the presence of pre-deformational diapirs could have intensified the frontal stagnation and controlled the geometry of the resulting olistostromic unit in the Central Betics (Figures 4, 5, and 8; Tables 1 and 2). Similar gravitational units have also been observed in other natural progressive arcs. Examples of that are: the Terravecchia Fm and Lower to Middle Pleistocene clastic units in the Calabrian arc (Di Maggio et al., 2017; Gugliotta & Morticelli, 2012), the Jarmlita-Proc formation and other gravitational slidings in the Carpathian arc (Jurewicz and Segit., 2018), and the molasse unit in the Sulaiman arc (Humayon et al., 1991; Figure 11b).

5. Conclusions

Irrespective of the detachment layer configuration, analog models of progressive arcs produce similar high protrusion values and strain partitioning into radial arc-perpendicular shortening, accommodated by thrusts, and arc-parallel stretching, accommodated by both normal and conjugate strike-slip faults.

- Any heterogeneity in the detachment layer conditions the wedge geometry as well as the nucleation, later evolution and kinematics of structures.
- The presence of diapirs favors the nucleation of normal and strike-slip faults, therefore localizing the along-strike segmentation of fold-and-thrust belts. Frontal deformation frequently stagnates at the diapirs, thus generating thick fold-and-thrust belts.
- Silicone bands arranged parallel to the apex movement generate distinctive structural styles along the fold-and-thrust belt. More frictional detachments produce thicker wedges and less frontal propagation. The

differential displacements between fold-and-thrust belt segments are accommodated by transfer zones oriented parallel to the apex movement.

- Silicone pinch-outs oriented perpendicular to the apex movement strongly localized the deformation front, which hardly propagates frontward. It favors wedge thickening that leads to frontal collapse and the subsequent deposition of gravitational-derived units.

These results can be useful to better understand how changes in the detachment layer configuration may influence the geometry and kinematics of natural fold-and-thrust belts that develop, at least partly, likeprogressive arcs, such as the Gibraltar arc, or the Sulaiman and the Zagros belts. Moreover, this work provides a positive starting point for future quantitative analysis that may evaluate the role of specific parameters and/or reproduce in detail natural cases of progressive arcs with heterogeneous, evaporitic-rich detachment layers.

Data Availability Statement

The videos of Models 1 to 7 supporting the conclusions can be obtained through Figshare data repository: https://figshare.com/account/home#/collections/6067796/add_items_mydata and also in Figure S1.

Acknowledgments
We thank the revisions made by the referees Stephen Marshak, Nemanja Krstekanic and Frank Zwaan that really contributed to improve this manuscript. This research is part of projects PGC2018-100914-B-I00, funded by the Ministerio de Ciencia e Innovación (Spanish Government)/AEI/10.13039/501100011033/ERDF; and Universidad Pablo de Olavide-1259543, funded by the Consejería de Economía, Conocimiento, Compañías y Universidad (Andalusian Government)/ERDF. Funding for open access publishing: Universidad Pablo de Olavide/CBUA.

References

Agarwal, K. K., & Agrawal, G. K. (2002). Analogue sandbox models of thrust wedges with variable basal frictions. *Gondwana Research*, *5*(3), 641–647. https://doi.org/10.1016/s1342-937x(05)70635-3

Allerton, S. (1998). Geometry and kinematics of vertical-axis rotations in fold and thrust belts. *Tectonophysics*, *299*(1–3), 15–30. https://doi.org/10.1016/s0040-1951(98)00196-6

Bahroudi, A., & Koyi, H. (2003). Effect of spatial distribution of Hormuz salt on deformation style in the Zagros fold and thrust belt: An analogue modelling approach. *Journal of the Geological Society*, *160*(5), 719–733. https://doi.org/10.1144/0016-764902-135

Balanyá, J. C., Crespo-Blanc, A., Díaz Azpiroz, M., Expósito, I., & Luján, M. (2007). Structural trend line pattern and strain partitioning around the Gibraltar Arc accretionary wedge: Insights as to the mode of orogenic arc building. *Tectonics*, *26*(2). https://doi.org/10.1029/2005tc001932

Barcos, L., Balanyá, J. C., Díaz-Azpiroz, M., Expósito, I., & Jiménez-Bonilla, A. (2015). Kinematics of the Torcal Shear Zone: Transpressional tectonics in a salient-recess transition at the northern Gibraltar Arc. *Tectonophysics*, *663*, 62–77. https://doi.org/10.1016/j.tecto.2015.05.002

Berástegui, X. C. C. C. D. M. A., Banks, C. J., Puig, C., Taberner, C., Waltham, D., & Fernández, M. (1998). Lateral diapiric emplacement of Triassic evaporites at the southern margin of the Guadalquivir Basin, Spain. *Geological Society, London, Special Publications*, *134*(1), 49–68. https://doi.org/10.1144/gsl.sp.1998.134.01.04

Burkhard, M., & Sommaruga, A. (1998). Evolution of the western Swiss Molasse basin: Structural relations with the Alps and the Jura belt. *Geological Society, London, Special Publications*, *134*(1), 279–298. https://doi.org/10.1144/gsl.sp.1998.134.01.13

Chalouan, A., Michard, A., El Kadiri, K., Negro, F., De Lamotte, D. F., Soto, J. I., & Saddiqi, O. (2008). The Rif Belt. In *Continental evolution: The geology of Morocco* (pp. 203–302). Springer.

Cifelli, F., Mattei, M., & Della Seta, M. (2008). Calabrian Arc oroclinal bending: The role of subduction. *Tectonics*, *27*(5). https://doi.org/10.1029/2008tc002272

Cobbold, P. R., Durand, S., & Mourgues, R. (2001). Sandbox modelling of thrust wedges with fluid-assisted detachments. *Tectonophysics*, *334*(3–4), 245–258. https://doi.org/10.1016/s0040-1951(01)00070-1

Costa, E., & Vendeville, B. C. (2002). Experimental insights on the geometry and kinematics of fold-and-thrust belts above weak, viscous evaporitic décollement. *Journal of Structural Geology*, *24*(11), 1729–1739. https://doi.org/10.1016/s0191-8141(01)00169-9

Cotton, J. T., & Koyi, H. A. (2000). Modelling of thrust fronts above ductile and frictional detachments: Application to structures in the salt range and Potwar Plateau, Pakistan. *The Geological Society of America Bulletin*, *112*(3), 351–363. 10.1130/0016-7606(2000)112<351:motfad>2.0.co;2

Couzens-Schultz, B. A., Vendeville, B. C., & Wiltschko, D. V. (2003). Duplex style and triangle zone formation: Insights from physical modeling. *Journal of Structural Geology*, *25*(10), 1623–1644. https://doi.org/10.1016/S0191-8141(03)00004-X

Crespo-Blanc, A. (2008). Recess drawn by the internal zone outer boundary and oblique structures in the paleomargin-derived units (Subbetic Domain, central Betics): An analogue modelling approach. *Journal of Structural Geology*, *30*(1), 65–80. https://doi.org/10.1016/j.jsg.2007.09.009

Crespo-Blanc, A., Balanyá, J. C., Expósito, I., Luján, M., & Suades, E. (2012). Crescent-like large-scale structures in the external zones of the western Gibraltar Arc (Betic–Rif orogenic wedge). *Journal of the Geological Society*, *169*(6), 667–679. https://doi.org/10.1144/jgs2011-115

Crespo-Blanc, A., Comas, M., & Balanyá, J. C. (2016). Clues for a Tortonian reconstruction of the Gibraltar Arc: Structural pattern, deformation diachronism and block rotations. *Tectonophysics*, *683*, 308–324. https://doi.org/10.1016/j.tecto.2016.05.045

Crespo Blanc, A., & Gálvez, E. (2008). Analogue modelling of non-cylindric fold-and-thrust belt around diapirs: Preliminary results.

Crespo Blanc, A., & González Sánchez, A. (2005). Influence of indenter geometry on arcuate fold-and-thrust wedge: Preliminary results of analogue modelling.

Crespo-Blanc, A., Jiménez-Bonilla, A., Balanyá, J. C., Expósito, I., & Díaz-Azpiroz, M. (2017). Influence of diapirs on the development of non-cylindrical arcuate fold-and-thrust belts: Results from analogue models of progressive arcs. *Geogaceta*, *61*.

Crespo-Blanc, A., Jiménez-Bonilla, A., Balanyá, J. C., Expósito, I., & Díaz-Azpiroz, M. (2018). From field data to lithospheric-scale models going through analogue experiments: The Gibraltar Arc system revisited in the light of the external zones structural evolution. *Revista de la Sociedad Geologica de Espana*, *31*, 111–122.

Dahlen, F. A. (1990). Critical taper model of fold-and-thrust belts and accretionary wedges. *Annual Review of Earth and Planetary Sciences*, *18*(1), 55–99. https://doi.org/10.1146/annurev.ea.18.050190.000415

Dahlen, F. A., Suppe, J., & Davis, D. (1984). Mechanics of fold-and-thrust belts and accretionary wedges: Cohesive Coulomb theory. *Journal of Geophysical Research*, *89*(B12), 10087–10101. https://doi.org/10.1029/jb089ib12p10087

Davis, D., Suppe, J., & Dahlen, F. A. (1983). Mechanics of fold-and-thrust belts and accretionary wedges. *Journal of Geophysical Research*, *88*(B2), 1153–1172. https://doi.org/10.1029/jb088ib02p01153

Di Maggio, C., Madonia, G., Vattano, M., Agnesi, V., & Monteleone, S. (2017). Geomorphological evolution of western Sicily, Italy. *Geologica Carpathica*, *68*(1), 80–93. https://doi.org/10.1515/geoca-2017-0007

Driehaus, L., Nalpas, T., Cobbold, P. R., Gelabert, B., & Sabat, F. (2013). Effects of margin-parallel shortening and density contrasts on back-arc extension during subduction: Experimental insights and possible application to Anatolia. *Tectonophysics*, *608*, 288–302. https://doi.org/10.1016/j.tecto.2013.09.028

Duffy, O. B., Dooley, T., Hudec, M. R., Fernandez, N., Jackson, C. A. L., & Soto, J. I. (2020). Structural evolution of salt-influenced fold-and-thrust belts: Principles in salt Basins containing isolated Minibasins. *Journal of Structural Geology*, *114*, 206–221.

Duffy, O. B., Dooley, T. P., Hudec, M. R., Jackson, M. P., Fernandez, N., Jackson, C. A., & Soto, J. I. (2018). Structural evolution of salt-influenced fold-and-thrust belts: A synthesis and new insights from basins containing isolated salt diapirs. *Journal of Structural Geology*, *114*, 206–221. https://doi.org/10.1016/j.jsg.2018.06.024

Funiciello, F., Faccenna, C., Giardini, D., & Regenauer-Lieb, K. (2003). Dynamics of retreating slabs: 2. Insights from three-dimensional laboratory experiments. *Journal of Geophysical Research*, *108*(B4). https://doi.org/10.1029/2001jb000896

Gautier, P., Brun, J. P., Moriceau, R., Sokoutis, D., Martinod, J., & Jolivet, L. (1999). Timing, kinematics and cause of Aegean extension: A scenario based on a comparison with simple analogue experiments. *Tectonophysics*, *315*(1–4), 31–72. https://doi.org/10.1016/s0040-1951(99)00281-4

Ghiglione, M. C., & Cristallini, E. O. (2007). Have the southernmost Andes been curved since Late Cretaceous time? An analog test for the Patagonian Orocline. *Geology*, *35*(1), 13–16. https://doi.org/10.1130/g22770a.1

Gilbert, E., & Merle, O. (1987). Extrusion and radial spreading beyond a closing channel. *Journal of Structural Geology*, *9*(4), 481–490. https://doi.org/10.1016/0191-8141(87)90123-4

Gugliotta, C., & Morticelli, M. G. (2012). Using high-resolution stratigraphy and structural analysis to constrain polyphase tectonics in wedge-top basins: Inferences from the late Tortonian Scillato Basin (central-northern Sicily). *Sedimentary Geology*, *273*, 30–47. https://doi.org/10.1016/j.sedgeo.2012.06.009

Hassanpour, J., Jahani, S., Ghassemi, M. R., Alavi, S. A., & Zeinali, F. (2018). Evolution of the Karebas Fault System and adjacent folds, central Zagros fold-and-thrust belt, Iran: Role of pre-existing halokinesis (salt structures and minibasins) and detachment levels. *Journal of Asian Earth Sciences*, *164*, 125–142. https://doi.org/10.1016/j.jseaes.2018.06.024

Hatzfeld, D., & Molnar, P. (2010). Comparisons of the kinematics and deep structures of the Zagros and Himalaya and of the Iranian and Tibetan Plateaus and geodynamic implications. *Reviews of Geophysics*, *48*(2), RG2005. https://doi.org/10.1029/2009rg000304

Hessami, K. (2002). Tectonic history and present-day deformation in the Zagros fold-thrust belt (Doctoral dissertation, Acta Universitatis Upsaliensis).

Hindle, D., & Burkhard, M. (1999). Strain, displacement and rotation associated with the formation of curvature in fold belts; the example of the Jura arc. *Journal of Structural Geology*, *21*(8–9), 1089–1101. https://doi.org/10.1016/s0191-8141(99)00021-8

Humayon, M., Lillie, R. J., & Lawrence, R. D. (1991). Structural interpretation of the eastern Sulaiman foldbelt and foredeep, Pakistan. *Tectonics*, *10*(2), 299–324. https://doi.org/10.1029/90tc02133

Jackson, J., Roberts, D. G., & Snelson, S. (1986). *Salt-tectonics*. Elservier.

Jadoon, I. A., Ding, L., Nazir, J., Idrees, M., & Saif-ur-Rehman, K. J. (2020). Structural interpretation of frontal folds and hydrocarbon exploration, western sulaiman fold belt, Pakistan. *Marine and Petroleum Geology*, *117*, 104380. https://doi.org/10.1016/j.marpetgeo.2020.104380

Jadoon, I. A., Lawrence, R. D., & Lillie, R. J. (1994). Seismic data, geometry, evolution, and shortening in the active Sulaiman fold-and-thrust belt of Pakistan, southwest of the Himalayas. *AAPG Bulletin*, *78*(5), 758–774.

Jiménez-Bonilla, A., Blanc, A. C., Roure, J. C. B., Expósito, I., & Díaz-Azpiroz, M. (2018). Brittle-ductile analogue models of fold-and-thrust belts developed during progressive arching: The effect of viscous basal layer pinch-outs. *Geogaceta*, *64*, 15–18.

Jiménez-Bonilla, A., Crespo-Blanc, A., Balanyá, J. C., Expósito, I., & Díaz-Azpiroz, M. (2017). Brittle-ductile analogue modelling of piedmont arcs: The influence of pushing-from-behind in gravity-driven models. *Bollettino di Geofisica Teorica ed Applicata*, *58*(1), 1–l5. https://doi.org/10.4430/bgta0187

Jiménez-Bonilla, A., Crespo-Blanc, A., Balanyá, J. C., Expósito, I., & Díaz-Azpiroz, M. (2020). Analog models of Fold-and-Thrust wedges in progressive arcs: A comparison with the Gibraltar arc external wedge. *Frontiers in Earth Science*. https://doi.org/10.3389/feart.2020.00072

Jiménez-Bonilla, A., Expósito, I., Balanyá, J. C., & Díaz-Azpiroz, M. (2017). Strain partitioning and relief segmentation in arcuate fold-and-thrust belts: A case study from the western Betics. *Journal of Iberian Geology*, *43*(3), 497–518. https://doi.org/10.1007/s41513-017-0028-0

Jiménez-Bonilla, A., Expósito, I., Balanyá, J. C., Díaz-Azpiroz, M., & Barcos, L. (2015). The role of strain partitioning on intermontane basin inception and isolation, External Western Gibraltar Arc. *Journal of Geodynamics*, *92*, 1–17. https://doi.org/10.1016/j.jog.2015.09.001

Jimenez-Bonilla, A., Torvela, T., Balanyá, J. C., Expósito, I., & Díaz-Azpiroz, M. (2016). Changes in dip and frictional properties of the basal detachment controlling orogenic wedge propagation and frontal collapse: The external central Betics case. *Tectonics*, *35*(12), 3028–3049. https://doi.org/10.1002/2016tc004196

Jurewicz, E., & Segit, T. (2018). The tectonics and stratigraphy of the transitional zone between the Pieniny Klippen Belt and Magura Nappe (Szczawnica area, Poland). *Geology, Geophysics and Environment*, *44*(1), 127. https://doi.org/10.7494/geol.2018.44.1.127

Kokinou, E., Kamberis, E., Kotsi, F., Lioni, K., & Velaj, T. (2017). he impact of evaporites in the Greek and Albanian oil systems. In *T79th EAGE Conference and Exhibition 2017* (Vol. 1, pp. 1–5). European Association of Geoscientists & Engineers.

Koyi, H. A., & Sans, M. (2006). Deformation transfer in viscous detachments: Comparison of sandbox models to the South Pyrenean Triangle Zone. *Geological Society, London, Special Publications*, *253*(1), 117–134. https://doi.org/10.1144/gsl.sp.2006.253.01.06

Letouzey, J. L. B. C. J., Colletta, B., Vially, R. A., & Chermette, J. C. (1995). Evolution of salt-related structures in compressional settings.

Li, J., & Mitra, S. (2017). Geometry and evolution of fold-thrust structures at the boundaries between frictional and ductile detachments. *Marine and Petroleum Geology*, *85*, 16–34. https://doi.org/10.1016/j.marpetgeo.2017.04.011

Lickorish, W. H., Ford, M., Burgisser, J., & Cobbold, P. R. (2002). Arcuate thrust systems in sandbox experiments: A comparison to the external arcs of the Western Alps. *The Geological Society of America Bulletin*, *114*(9), 1089–1107. https://doi.org/10.1130/0016-7606(2002)114<1089:atsise>2.0.co;2

Lillie, R. J. (1991). Evolution of gravity anomalies across collisional mountain belts: Clues to the amount of continental convergence and underthrusting. *Tectonics*, *10*(4), 672–687. https://doi.org/10.1029/91tc00356

Livani, M., Scrocca, D., Arecco, P., & Doglioni, C. (2018). Structural and stratigraphic control on salient and recess development along a thrust belt front: The Northern Apennines (Po Plain, Italy). *Journal of Geophysical Research: Solid Earth*, *123*(5), 4360–4387. https://doi.org/10.1002/2017jb015235

Macedo, J., & Marshak, S. (1999). Controls on the geometry of fold-thrust belt salients. *The Geological Society of America Bulletin*, *111*(12), 1808–1822. https://doi.org/10.1130/0016-7606(1999)111<1808:cotgof>2.3.co;2

Marshak, S. (1988). Kinematics of orocline and arc formation in thin-skinned orogens. *Tectonics*, *7*(1), 73–86. https://doi.org/10.1029/tc007i001p00073

Marshak, S. (2004). Arcs, Oroclines, Salients, and Syntaxes-The origin of map-view curvature in fold-thrust belts. In K. R. McClay (Ed.), *Thrust Tectonics and Petroleum Systems: American Association of Petroleum Geologists Memoir* (Vol. *82*, pp. 131–156).

Marshak, S., Geiser, P., Alvarez, W., & Engelder, T. (1982). Mesoscopic fault array of northern Umbrian Apennine fold belt, Italy: Geometry of conjugate shear by pressure-solution slip. *The Geological Society of America Bulletin*, *93*(10), 1013–1022. https://doi.org/10.1130/0016-7606(1982)93<1013:mfaotn>2.0.co;2

Martínez del Olmo, W., Motis, K., & Martín, D. (2015). El papel del diapirismo de la sal Triásica en la estructuración del Prebético (SE de España). *Revista de la Sociedad Geologica de Espana*, *28*(1), 3–24.

McQuarrie, N. (2004). Crustal scale geometry of the Zagros fold–thrust belt, Iran. *Journal of Structural Geology*, *26*(3), 519–535. https://doi.org/10.1016/j.jsg.2003.08.009

Merle, O. (1986). Patterns of stretch trajectories and strain rates within spreading-gliding nappes. *Tectonophysics*, *124*(3–4), 211–222. https://doi.org/10.1016/0040-1951(86)90201-5

Merle, O. (1989). Strain models within spreading nappes. *Tectonophysics*, *165*(1–4), 57–71. https://doi.org/10.1016/0040-1951(89)90035-8

Najafi, M., Vergés, J., Etemad-Saeed, N., & Karimnejad, H. R. (2018). Folding, thrusting and diapirism: Competing mechanisms for shaping the structure of the north Dezful Embayment, Zagros, Iran. *Basin Research*, *30*(6), 1200–1229.

Nieto, L. M., Molina, J. M. y., & Ruíz-Ortíz, P. A. (1992). Influencia de la tectónica de fractura y del diapirismo en la sedimentación del Jurásico y Cretácico basal al Sur de la provincia de Jaén (Zona Subbética). *Revista de la Sociedad Geologica de Espana*, *5*, 95–112.

Nilforoushan, F., & Koyi, H. A. (2007). Displacement fields and finite strains in a sandbox model simulating a fold-thrust-belt. *Geophysical Journal International*, *169*(3), 1341–1355. https://doi.org/10.1111/j.1365-246x.2007.03341.x

Pastor-Galán, D., Gutiérrez-Alonso, G., Zulauf, G., & Zanella, F. (2012). Analogue modeling of lithospheric-scale orocline buckling: Constraints on the evolution of the Iberian-Armorican Arc. *The Bulletin*, *124*(7–8), 1293–1309. https://doi.org/10.1130/b30640.1

Pedrera, A., Marín-Lechado, C., Galindo-Zaldívar, J., & García-Lobón, J. L. (2014). Control of preexisting faults and near-surface diapirs on geometry and kinematics of fold-and-thrust belts (Internal Prebetic, Eastern Betic Cordillera). *Journal of Geodynamics*, *77*, 135–148. https://doi.org/10.1016/j.jog.2013.09.007

Reynolds, K., Copley, A., & Hussain, E. (2015). Evolution and dynamics of a fold-thrust belt: The Sulaiman Range of Pakistan. *Geophysical Journal International*, *201*(2), 683–710. https://doi.org/10.1093/gji/ggv005

Roca, E., Sans, M., & Koyi, H. A. (2006). Polyphase deformation of diapiric areas in models and in the eastern Prebetics (Spain). *AAPG Bulletin*, *90*(1), 115–136. https://doi.org/10.1306/07260504096

Roldán García, F. J., Rodríguez Fernández, J., & Azañón, J. M. (2012). La Unidad Olistostrómica, una formación clave para entender la historia neógena de las Zonas Externas de la Cordillera Bética.

Rowan, M. G., & Vendeville, B. C. (2006). Foldbelts with early salt withdrawal and diapirism: Physical model and examples from the northern Gulf of Mexico and the Flinders Ranges, Australia. *Marine and Petroleum Geology*, *23*(9–10), 871–891. https://doi.org/10.1016/j.marpetgeo.2006.08.003

Rubinat, M., Roca, E., Escalas, M., Queralt, P., Ferrer, O., & Ledo, J. J. (2013). The influence of basement structure on the evolution of the Bicorb-Quesa Diapir (eastern Betics, Iberian Peninsula): Contractive thin-skinned deformation above a pre-existing extensional basement fault. *International Journal of Earth Sciences*, *102*(1), 25–41. https://doi.org/10.1007/s00531-012-0789-9

Ruh, J. B., Gerya, T., & Burg, J. P. (2017). Toward 4D modeling of orogenic belts: Example from the transpressive Zagros Fold Belt. *Tectonophysics*, *702*, 82–89. https://doi.org/10.1016/j.tecto.2015.09.035

Ruh, J. B., Kaus, B. J., & Burg, J. P. (2012). Numerical investigation of deformation mechanics in fold-and-thrust belts: Influence of rheology of single and multiple décollements. *Tectonics*, *31*(3). https://doi.org/10.1029/2011tc003047

Sans, M. (2003). From thrust tectonics to diapirism. The role of evaporites in the kinematic evolution of the eastern South Pyrenean front. *Geológica Acta*, *1*(3), 239–260.

Sanz de Galdeano, C., Galindo Zaldivar, J., Lopez-Garrido, A. C., Alfaro, P., Perez-Valera, F., Perez-Lopez, A., & Garcia Tortosa, F. J. (2006). The fault of Tiscar: Its meaning in the southwest termination of the Prebetical arc. *Revista de la Sociedad Geológica de España*, *19*, 271–280.

Schellart, W., & Strak, V. (2016). A review of analogue modelling of geodynamic processes: Approaches, scaling, materials and quantification, with an application to subduction experiments. *Journal of Geodynamics*, *100*, 7–32. https://doi.org/10.1016/j.jog.2016.03.009

Schellart, W. P., Lister, G. S., Sussman, A. J., & Weil, A. B. (2004). Tectonic models for the formation of arc-shaped convergent zones and Backarc Basins. *Orogenic Curvature: Integrating Paleomagnetic and Structural Analyses*, *383*, 237–258. https://doi.org/10.1130/0-8137-2383-3(2004)383[237:TMFTFO]2.0.CO;2

Sepehr, M., & Cosgrove, J. W. (2005). Role of the Kazerun Fault Zone in the formation and deformation of the Zagros fold-thrust Belt, Iran. *Tectonics*, *24*(5). https://doi.org/10.1029/2004tc001725

Turtù, A., Satolli, S., Maniscalco, R., Calamita, F., & Speranza, F. (2013). Understanding progressive-arc-and strike-slip-related rotations in curve-shaped orogenic belts: The case of the Olevano-Antrodoco-Sibillini thrust (Northern Apennines, Italy). *Journal of Geophysical Research: Solid Earth*, *118*(2), 459–473. https://doi.org/10.1002/jgrb.50096

Vera, J. A. (Ed.) (2004). *Geología de españa*.

Weil, A. B., & Sussman, A. J. (2004). Classifying curved orogens based on timing relationships between structural development and vertical-axis rotations. *Orogenic Curvature: Integrating Paleomagnetic and Structural Analyses*, *383*, 1–15. https://doi.org/10.1130/0-8137-2383-3(2004)383[1:CCOBOT]2.0.CO;2

Wu, J. E., & McClay, K. R. (2011). Two-dimensional analog modeling of fold and thrust belts: Dynamic interactions with syncontractional sedimentation and erosion.

Yonkee, W. A., & Weil, A. B. (2015). Tectonic evolution of the Sevier and Laramide belts within the North American Cordillera orogenic system. *Earth-Science Reviews*, *150*, 531–593. https://doi.org/10.1016/j.earscirev.2015.08.001